NASA TECHNICAL NOTE

NASA TN D-4791

NASA TN D-4791

FLIGHT INVESTIGATION OF THE EFFECTS OF APOLLO HEAT-SHIELD SINGULARITIES ON ABLATOR PERFORMANCE

by Thomas E. Walton, Jr., William G. Witte, and Brian J. O'Hare

Langley Research Center
Langley Station, Hampton, Va.

NATIONAL AERONAUTICS AND SPACE ADMINISTRATION • WASHINGTON, D. C. • SEPTEMBER 1968

FLIGHT INVESTIGATION OF THE EFFECTS OF APOLLO HEAT-SHIELD SINGULARITIES ON ABLATOR PERFORMANCE

By Thomas E. Walton, Jr., William G. Witte, and Brian J. O'Hare

Langley Research Center
Langley Station, Hampton, Va.

NATIONAL AERONAUTICS AND SPACE ADMINISTRATION

For sale by the Clearinghouse for Federal Scientific and Technical Information
Springfield, Virginia 22151 – CFSTI price $3.00

FLIGHT INVESTIGATION OF THE EFFECTS OF APOLLO HEAT-SHIELD SINGULARITIES ON ABLATOR PERFORMANCE

By Thomas E. Walton, Jr., William G. Witte,
and Brian J. O'Hare
Langley Research Center

SUMMARY

A flight investigation was conducted to evaluate the performance of the Apollo ablative heat-shield material under perturbed heating conditions caused by several simulated Apollo heat-shield singularities. The recovered spacecraft, which contained simulations of the Apollo singularities, experienced an order-of-magnitude less recession in the unperturbed areas than had been predicted. A recalculation of the surface recession utilizing revised rate-controlled oxidation constants obtained from arc-jet tests produced results compatible with the measured surface recession. With the exception of the upstream lip of both simulated umbilical fairings, no appreciable increase in surface recession attributable to the singularities was noted. The effects of simulated Apollo singularities on ablator performance were minor, as evidenced from the recovered spacecraft.

INTRODUCTION

The Apollo command module contains some 15 major surface irregularities (singularities), such as protuberances, cavities, and gaps, that are integral parts of the heat shield. These include compression pads, shear pads, abort-tower wells, tension ties, intercompartmental gaps, access doors and hatches, antennas, umbilical fairings, reaction-control jets, and so forth (see fig. 1). The presence of these singularities in the heat shield can increase the heating in their vicinity by an order of magnitude (see refs. 1 and 2). In these regions of perturbed heating, severe degradation of the Apollo heat-shield material might result.

It was recognized that this problem could not be investigated and resolved with any degree of confidence in ground facilities alone; hence, at the request of the NASA Manned Spacecraft Center, the present investigation was initiated to provide an intermediate step between ground tests and Apollo flight tests utilizing a Pacemaker launch vehicle (four-stage, solid-propellant, unguided vehicle). The present experiment consisted of flight

testing a recoverable spacecraft containing simulations of Apollo heat-shield singularities – specifically, the leeward ramp-umbilical combination, a leeward recessed compression pad, and the windward umbilical cavity.

This paper presents the results obtained from the flight investigation along with an evaluation of the effects of perturbed heating on the ablative-material performance due to the presence of singularities in the heat shield.

SYMBOLS

A	frequency factor, $lbm/ft^2\text{-}sec\text{-}atm^{0.7}$ $\left(kg/m^2\text{-}sec\text{-}atm^{0.7}\right)$
ΔE	activation energy, Btu/lbm (J/mole)
e	base of natural system of logarithms (2.71828)
h	cavity depth, in. (cm)
K_O	oxygen mass fraction
l	cavity length, in. (cm)
M	Mach number
$\dot{m}$	mass loss rate, $lbm/ft^2\text{-}sec$ $(kg/m^2\text{-}sec)$
n	exponent in Arrhenius equation
p	pressure, atm
R	universal gas constant, Btu/lbm-^oR (J/mole-^oK)
r_n	nose radius, in. (cm)
N_{Re}	Reynolds number per foot (per 30.48 cm)
s	surface distance along body measured from stagnation point, in. (cm)
T	temperature, ^oR (^oK)

w	cavity width, in. (cm)
δ	boundary-layer thickness, in. (cm)
ρ	density, lbm/ft^3 (kg/m^3)

Subscripts:

A	Apollo spacecraft
e	outer edge of boundary layer
P	Pacemaker spacecraft
SL	sea level
t	total condition
w	wall
∞	free stream
1	upstream
2	downstream

SPACECRAFT

Selection of Spacecraft Configuration

The configuration chosen for the spacecraft (see fig. 2) was a hemisphere-cone-cylinder of which the cylindrical section was utilized for the placement of the singularity simulations. Hereinafter this spacecraft is referred to as the Pacemaker spacecraft. It was recognized that a scaled model of the Apollo spacecraft would have produced a more desirable flow field for the experiment; however, the shear stress over the blunt face would have been an order of magnitude greater than the level experienced on the Apollo spacecraft because of trajectory limitations imposed by the Pacemaker launch vehicle. In this environment, severe degradation of the Apollo heat-shield material would result because the shear-sensitive threshold of the ablator (15 lbf/ft^2 or 718 N/m^2) would have been exceeded. This statement is borne out by the results of a previous Pacemaker

flight test reported in reference 3. Hence, the cylindrical section of the spacecraft was utilized for the placement of the singularity simulations, since the resulting environment more closely simulates the Apollo environment.

Design of Pacemaker Singularities

The objective of this test, given the fact that heating rates in the immediate vicinity of the singularities are increased to two or more times the undisturbed values, was to determine what local increases in surface recession result. By comparing the recession rates experienced in the disturbed and undisturbed regions at the time of closest simulation, a "recession factor" may be assigned to each singularity. The recession factors might then be compared with the heating factors to determine the relationship between the two. One point of considerable concern was the possibility that the increased heating would be accompanied by an increase in shear (Reynolds analogy) which in turn could cause recession rates considerably higher than would be predicted on the basis of the heating-rate increase alone.

To simulate the perturbed heating factors which are encountered by the Apollo spacecraft, the Pacemaker experiment design employed the method reported in reference 4. This method relates the local flow properties to the singularity geometry. For flow over a cavity, reference 4 shows that the ratio of boundary-layer thickness to cavity depth δ/h and the ratio of cavity length to cavity depth l/h are the pertinent similarity ratios. It is further shown that for either laminar or turbulent flow, these similarity ratios are essentially independent of Mach number and Reynolds number. Hence

$$(\delta/h)_P = (\delta/h)_A$$

and

$$(l/h)_P = (l/h)_A$$

Pertinent dimensions and similarity ratios for each singularity on both the Apollo and Pacemaker spacecraft are listed in table I. Table I shows that the boundary layer for the compression pad is turbulent on both Pacemaker and Apollo and that the dimensions for the compression pad on Pacemaker are scaled to approximately five-twelfths of the dimensions for the compression pad on Apollo. Figure 3(a) is a sketch of the compression pad on the Pacemaker spacecraft showing the pertinent details and dimensions.

For the windward umbilical cavity, table I indicates that the flow on Apollo is laminar whereas the flow on Pacemaker is turbulent. Because the boundary-layer types differ on the two spacecraft, a true simulation was not considered feasible. Nevertheless, the sizing of the windward umbilical cavity was accomplished by applying the aforementioned similarity relations and assuming turbulent-flow conditions on Pacemaker and laminar-flow conditions on Apollo. The application of the similarity relations was further

complicated because of the size limitation of the Pacemaker spacecraft. The length of the cavity l should have been approximately 7 inches (18 cm) on the Pacemaker spacecraft; however, l was limited to 3 inches (7.62 cm) so that ample space would be available for ablation sensors downstream of the cavity (see table I). Consequently, the ratio δ/h was 0.963 for Pacemaker as opposed to 0.415 for Apollo. The ratio of l/h was maintained constant from Apollo to Pacemaker, since, according to reference 4, the magnitude of this ratio determines whether the flow is separated or attached to the floor of the cavity. Figure 3(b) shows the pertinent details and dimensions of the windward-umbilical-cavity simulation.

Because of the complex geometry of the ramp-umbilical combination on the Apollo spacecraft, a simplified configuration that would lend itself to analytical treatment was assumed. Shown in figure 4 is a sketch where the solid lines represent the ramp-umbilical combination as it exists on Apollo and the dashed lines represent the ramp-umbilical combination as the assumed configuration for scaling from Apollo to Pacemaker. The floor between the ramp and the umbilical fairing is a curved surface on the Apollo spacecraft; however, the floor was assumed to be flat on the simplified configurations. Since the flow will separate over the floor according to unpublished wind-tunnel tests conducted at the Langley Mach 8 variable-density hypersonic tunnel, the floor geometry has no significant effect on the flow either internal or external to the cavity.

The aforementioned similarity relations were applied to the assumed ramp-umbilical configuration. Pertinent dimensions for the ramp-umbilical simulation on Pacemaker are listed in table I. Upon examination of table I, it is seen that the boundary-layer type for both Pacemaker and Apollo is turbulent. The ratio of the ramp height to umbilical height h_1/h_2 was maintained constant from Apollo to Pacemaker. The angles between the assumed flat floor and the ramp face and between the assumed flat floor and the umbilical face (57° and 56°, respectively) were maintained constant from Apollo to Pacemaker. Shown in figure 5 is a sketch of the simulated ramp-umbilical configuration on the Pacemaker spacecraft. Photographs of the Pacemaker spacecraft singularities are shown in figure 6.

Pacemaker Spacecraft Fabrication

The Pacemaker spacecraft consisted of three separate assemblies; the first assembly was a phenolic-carbon hemispherical nose cap bonded to a 0.078-inch-thick (0.198-cm) inconel substructure. This ablator material was chosen for the nose-cap heat shield because it had been extensively tested in ground facilities and had proven to be capable of surviving the severe environment (high heating rates and high stagnation pressure) encountered during reentry on the Pacemaker vehicle system with only minimal changes in geometry.

The remaining two assemblies of the spacecraft (the conical and cylindrical sections) were covered with Apollo ablator materials. These materials and the fabrication methods employed were identical to those developed for the Apollo spacecraft, with the one exception that no pore sealer was applied to the surface of the ablator. In reference 3 the pore sealer had been found to penetrate the ablator surface and therefore change its ablation-performance characteristics. The prime ablator material on the Apollo spacecraft is a filled epoxy-novolac resin system in a fiber-glass honeycomb matrix; however, the honeycomb reinforcement is eliminated where difficulty is encountered in forming the honeycomb around either complex shapes or around a curved surface having a small radius of curvature. Under these conditions, the epoxy-novolac resin system is molded into blocks and the blocks are machined to the complex shapes.

The second assembly consisted of the Apollo molded ablator bonded to a 0.043-inch-thick (0.109-cm) 10° conical substructure made of inconel. To be consistent with the experiment requirement, only the separation ramp upstream of the umbilical fairing required the molded ablator; however, since the maximum flight shear stress on the conical section approaches the level at which the honeycomb ablator is shear sensitive, the entire section was made of molded ablator which is more shear resistant than the honeycomb ablator.

The third assembly was a cylindrical configuration consisting of a composite of the Apollo honeycomb and molded ablators (the outer layer was fabricated from the honeycomb ablator and the sublayer from the molded ablator) bonded to a 0.043-inch-thick (0.109-cm) inconel substructure for three of the four quadrants. The remaining quadrant consisted entirely of the molded ablator, which was bonded directly to the substructure.

The reason for incorporating the sublayer of molded ablator on the Pacemaker substructure was to provide further protection around the geometric singularities, since the heating factors and consequently the shear stress in these areas were not clearly defined at the time the Pacemaker spacecraft was designed.

Simulations of the Apollo singularities were incorporated on the Pacemaker spacecraft. Scaled simulations of the leeward recessed compression pad and the windward umbilical cavity, shown in figure 3, were placed on the cylindrical portion of the spacecraft in two opposed quadrants of the composite honeycomb-molded ablator. Two scaled simulations of the leeward ramp-umbilical combination, shown in figure 5, were placed in the two remaining quadrants (one being located in the composite-ablator quadrant, the other in the molded-ablator quadrant). The recessed compression pad was made of a laminate of phenolic—fiber-glass material with the lamination edges exposed to the flow and was both bonded and mechanically fastened to the substructure. The windward umbilical cavity was made of a molding of phenolic-resin and randomly oriented glass fibers and was fastened to the substructure in the same manner as the compression pad. The

ramp-umbilical simulation located in the molded-ablator quadrant was made entirely of molded ablator. The ramp-umbilical simulation located in the composite-ablator quadrant was made of molded ablator with the exception of the floor located between the ramp and the umbilical fairing. This area was made of honeycomb ablator, as shown in figure 2, to simulate the Apollo condition. The materials tested and their characteristics are summarized in table II.

Instrumentation

The selection and location of instrumentation was based on obtaining the maximum amount of information during the brief period on the Pacemaker trajectory when the environment simulates the Apollo environment. Most of the instrumentation was located in the vicinity of the singularity simulations. Forty-eight ablation-event sensors of the type designed to measure surface recession were commutated on three ablation data channels and were recorded approximately every 0.025 second. Forty-four of these sensors were of the spring-wire type and four were of the light-pipe type. The development and method of operation of these sensors are described in reference 5. Figure 7 and table III show the ablation-sensor locations. Twenty-two thermocouples were commutated on two temperature channels and were recorded approximately every 0.067 second. Of the 12 thermocouples which were located in the cylindrical section of the spacecraft, four were fastened to the substructure (one each for each of the four quadrants) in the vicinity of the singularity simulations, three were located in the windward umbilical cavity at different depths, two were located in the leeward compression pad at different depths, and three were located at the interface of the composite honeycomb-molded quadrants (one each for each composite quadrant). All indepth thermocouples were assembled in removable plugs. Figure 7 and table IV show the locations of the 12 thermocouples in the cylindrical section. The remaining 10 thermocouples were located in other regions of the spacecraft – that is, on the conical substructure and the hemispherical nose cap.

As mentioned previously, the regions most heavily instrumented were in the areas of the singularity simulation; however, to obtain ablator-performance information on the undisturbed regions of the spacecraft cylinder, sensors 25 to 27 and 28 to 30 (see fig. 7) were located away from the singularities in the composite honeycomb-molded ablator and all-molded ablator, respectively.

A nine-channel telemeter, located just ahead of the fourth-stage rocket motor, was used to transmit three channels of ablation data, two channels of temperature data, and four channels of spacecraft-acceleration data.

FLIGHT-TEST RESULTS AND DISCUSSION

Launch Vehicle and Trajectory

The spacecraft was flight-tested from Wallops Station, Wallops Island, Virginia, with the use of an unguided Pacemaker launch vehicle. The propulsion system consisted of four stages of solid-propellant rocket motors. The first- and second-stage motors were an Honest John and a Nike, respectively, while the third- and fourth-stage motors were a TX77 and a Recruit, respectively. A photograph of the spacecraft and the launch vehicle is shown in figure 8.

The desired trajectory for this flight test was obtained by igniting the first two stages during vehicle ascent, and the last two stages during descent. The velocity at fourth-stage burnout was 10 113 ft/sec (3.082 km/sec) at an altitude of 73 992 feet (22.553 km). Upon examination of the telemetered data from the normal and transverse accelerometers in the spacecraft, no apparent body motions were noted during the data period. The recovery sequence began when the spacecraft and fourth stage coasted to an altitude of approximately 10 000 feet (3.048 km). At this point the spacecraft was separated from the fourth stage by a pyrotechnic device which was initiated by a barometric switch. A parachute was then deployed and the spacecraft was lowered to the water at a velocity of about 60 ft/sec (18.3 m/sec) 55 nautical miles (102 km) from Wallops Station. A plot of the flight trajectory and the sequence of events are shown in figure 9. The time histories of velocity and altitude during the data period for the Pacemaker flight are shown in figure 10. Trajectory data were obtained from the AN/FPQ-6 tracking radar.

Test Environment

The variation of free-stream Mach number and Reynolds number per foot (per 30.48 cm) during the data period is shown in figure 11. Atmospheric data (pressure, density, and temperature) obtained from radiosonde measurements are presented in figure 12.

Pressure distributions over the Pacemaker configuration are shown in figure 13 for several free-stream Mach numbers. These distributions were generated by the single-strip method presented in reference 6 and the method of characteristics.

The stagnation-point heating rate on the Pacemaker nose is shown in figure 14. Time histories of the heating rate, shear stress, Reynolds number, and pressure at two locations on the Pacemaker cone $\left(s/r_n = 1.6 \text{ and } 3.0\right)$ are shown in figure 15. The unperturbed heating rate, shear stress, pressure, Reynolds number, and Mach number on the Pacemaker cylinder $\left(s/r_n = 3.9\right)$ are shown in figure 16 as a function of time. All computations (i.e., heating rate, shear stress, etc.) on Pacemaker were made by utilizing

the same methods described in reference 3. For comparison, the unperturbed heating rate, shear stress, pressure, Reynolds number, and Mach number in the three areas of interest (compression pad, ramp-umbilical combination, and windward umbilical cavity) on the Apollo spacecraft are also shown in figure 16. Listed in table V are the pertinent similarity parameters for both the Pacemaker and Apollo environment at the time of simulation – that is, when the heating rate is a maximum during the second heating period for Apollo and at fourth-stage burnout (85.6 seconds) for Pacemaker.

Recession Measurements

During the course of the flight test only three of the 44 spring-wire sensors located in the vicinity of the simulated singularities actuated. These three sensors were located on the upstream lip of the umbilical simulation, the highest heating area instrumented. Although the sensors not on the umbilical simulation were arrayed at depths as small as 0.030 inch (0.0762 cm), none of these were even exposed during the course of the test. Of the four light-pipe sensors located immediately downstream of the simulated compression pad, none actuated during the test. A list of the ablation-event sensors that were exposed at the end of the flight test is presented in the following table:

Sensor no.	Quadrant, deg	Depth		Time actuated
		in.	cm	
19	90 to 180	0.030	0.076	Not actuated
20	↓	.104	.264	Not actuated
45	270 to 360	.038	.097	92.60 sec
46	↓	.102	.259	(*)
47	↓	.159	.404	Not actuated
48	↓	.060	.152	100.55 sec

*After spacecraft separated from telemetry system.

The conflicting performance of these sensors has not, as yet, been explained satisfactorily. This conflict, however, is of no consequence to the conclusions drawn herein.

From an experimental standpoint, the unexpectedly high performance of the ablator meant that no direct measurements of recession rates were obtained at the simulation time. The spacecraft, however, was recovered after the flight test (see fig. 17), and several conclusions can be drawn from the postflight recession measurements.

Measurements of the preflight and postflight surface locations in the areas of interest along the cylindrical section of the spacecraft and every 30° around the periphery of the spacecraft (see fig. 18) were made by means of a dial gage and measuring fixture modified for this application. The surface recession experienced by the spacecraft is

shown in figure 19. The ordinate should not be taken as absolute ablator thickness, since use of the dial gage did not permit such a measurement. The surface recession is represented by the distance between the preflight and postflight measurements. It is obvious, upon examination of these figures, that the postflight surface was highly irregular. The irregularities in the surface were due to the tendency of the honeycomb matrix to recede at a slower rate than the resin system itself.

A comparison between some typical measured unperturbed values of surface recession and the predicted values computed by the method described in reference 7 is presented in the following table:

Ablator material and location	Surface recession			
	Calculated		Measured	
	in.	cm	in.	cm
Molded ablator on cone $(s/r_n = 1.6)$	0.52	1.32	0.020 to 0.040	0.051 to 0.102
Composite ablator on cylinder	.232	.590	.005 to .015	.0127 to .0381
Molded ablator on cylinder	.210	.533	.002 to .015	.0051 to .0381

The order-of-magnitude difference between predicted and actual recession led, at first, to concern over the assumption that the boundary layer had been turbulent during the test period. A recalculation of recession based upon the unlikely assumption that the flow was laminar (i.e., Reynolds number on cylindrical section was greater than 400 000 at 85.6 seconds) through the test period failed to produce recession predictions close to the measurements.

In order to find the explanation for the low surface recession experienced in flight, a reexamination of the behavior of the Apollo ablators, particularly at low temperatures (less than 3500° R or 1944° K), was undertaken. The rate-controlled oxidation equation for these materials was of primary interest in this investigation. The investigation consisted of a series of arc-jet tests using 2-inch-diameter (5.08-cm) models (see fig. 20). The primary data collected during the tests were surface-recession rate and surface temperature. Surface-recession rate was obtained by dividing the total measured recession by the model exposure time. The surface-temperature history was measured by means of a photographic pyrometer developed at Langley Research Center. The operation of this instrument is described in reference 8. All tests were conducted in the Langley 20-inch hypersonic arc-heated tunnel, which is described in reference 9. Stagnation pressures $(p_{t,2})$ for these tests ranged from 0.075 atm to 0.14 atm (1 atm = 101 325 N/m^2). Air was the test medium for all tests.

The data from this series of tests were reduced and plotted to obtain constants for the Arrhenius equation

$$\dot{m} = A\left(K_{O,e}p_e\right)^n e^{-\Delta E/RT}$$

In order to convert the surface-recession rate to the mass loss rate $\dot{m}$, a char density of 15.68 lbm/ft^3 (251.2 kg/m^3) was used for the honeycomb material and 17.95 lbm/ft^3 (287.6 kg/m^3) for the molded material. These values were based on the measured virgin density of the materials and char-yield fractions obtained from thermogravimetric analysis. The resultant Arrhenius plots are shown in figure 21, where the value of n was taken as 0.7 to best collapse the data onto a straight line. Although it is possible to fair a number of straight lines through the data in figure 21, any fairing which is representative of the data will produce a set of constants that is accurate within the temperature range of the data. The Arrhenius constants for both the honeycomb and molded ablator materials are tabulated as follows:

Ablator	A		ΔE/R	
	lb/ft^2-sec-atm$^{0.7}$	kg/m^2-sec-atm$^{0.7}$	^oR	^oK
Honeycomb	0.180	0.877	7360	4080
Molded	.171	.833	↓	↓

Figure 22 shows a comparison between the Arrhenius equation obtained from the arc-jet data and the equation supplied by the manufacturer of the honeycomb material. The comparison between the two was based on a local pressure p_e of 0.1 atm and an oxygen mass fraction $K_{O,e}$ of 0.232. It should be noted that, even at low temperatures, there is an order-of-magnitude difference between the two. A comparison between the measured surface recession and the surface recession calculated by utilizing the revised Arrhenius constants is shown in the following table:

Ablator material and location	Surface recession			
	Calculated		Measured	
	in.	cm	in.	cm
Molded ablator on cone $(s/r_n = 1.6)$	0.035	0.089	0.020 to 0.040	0.051 to 0.102
Composite ablator on cylinder	.0135	.0343	.005 to .015	.0127 to .0381
Molded ablator on cylinder	.0130	.033	.002 to .015	.0051 to .0381

It can be seen that the arc-jet tests produced results compatible with the measured recession. As a further check on the revised Arrhenius constants obtained from the arc-jet data, the computed char thickness for the honeycomb material on the cylindrical section was 0.075 inch (0.191 cm) as opposed to the measured value of 0.090 inch (0.229 cm).

Interference Effects on Ablator Performance

By comparing the recession experienced by the ablator in the undisturbed areas with the recession experienced in the vicinity of the singularities, the reader can note that there was no appreciable increase in recession attributable to the singularities. The sole exception to this statement was the behavior of the material on the upstream lip of both simulated umbilical fairings (see figs. 23 and 24). These areas experienced local heating rates far more severe than did any of the other singularities. Although the area of concern in the ramp-umbilical simulation was between and around the protrusions, the upstream lip of the umbilical simulation and the downstream edge of the ramp simulation were instrumented with spring-wire sensors to monitor their geometry during the test. In the area of concern (the area between the ramp and umbilical simulations), there was increased heating caused by the singularities, as evidenced by the char color and char depth (see figs. 23 and 24). In this area, however, any increase in surface recession which may have occurred falls within the variations in recession measured in the undisturbed flow regions. Similar observations were made in the other areas of concern – that is, downstream of the windward-umbilical-cavity simulation and compression-pad simulation (see figs. 25, 26, and 27).

As mentioned previously, both the windward-umbilical-cavity simulation and the compression-pad simulation were instrumented with thermocouples that were imbedded in the material at several depths. Figures 28 and 29 show the time histories of the temperature at several depths in both the simulations as determined from the indepth thermocouples. Although the maximum temperature at a depth of 0.1 inch (0.254 cm) (thermocouple no. 2) in the windward-umbilical-cavity simulation was 900° R (500° K), local melting on the downstream fiber-glass lip can be seen in figure 25. Similar results are also seen on the downstream lip of the compression pad (see fig. 26). Thermocouples located both on the substructure and at the interface of the composite-ablator quadrants recorded no rise in temperature during the entire flight.

CONCLUDING REMARKS

A flight investigation was conducted to evaluate the performance of the Apollo ablative heat-shield material under perturbed heating conditions caused by several simulated Apollo heat-shield singularities. Of major significance was the order-of-magnitude difference between predicted and actual surface recession experienced by the ablative heat

shield in both the perturbed and unperturbed regions of the spacecraft. A recalculation of the surface recession utilizing revised rate-controlled oxidation constants obtained from arc-jet tests produced results compatible with the measured surface recession. Postflight inspection of the simulated singularities and of the heat shield in the regions of the simulated singularities showed no appreciable increase in recession attributable to perturbed heating; however, the upstream lips of both umbilical fairings were eroded slightly. The effects of singularities on the performance of the Apollo ablative heat-shield material were found to be minor in the present flight investigation.

Langley Research Center,
National Aeronautics and Space Administration,
Langley Station, Hampton, Va., June 24, 1968,
709-09-00-01-23.

REFERENCES

1. Jones, Robert A.; and Hunt, James L.: Effects of Cavities, Protuberances, and Reaction-Control Jets on Heat Transfer to the Apollo Command Module. NASA TM X-1063, 1965.

2. Hunt, James L.; and Jones, Robert A.: Effects of Several Ramp-Fairing, Umbilical, and Pad Configurations on the Aerodynamic Heating to the Apollo Command Module at Mach 8. NASA TM X-1640, 1968.

3. Graves, Randolph A., Jr.; and Witte, William G.: Flight-Test Analysis of Apollo Heat-Shield Material Using the Pacemaker Vehicle System. NASA TN D-4713, 1968.

4. Charwat, A. F.; Roos, J. N.; Dewey, F. C., Jr.; and Hitz, J. A.: An Investigation of Separated Flows – Part I: The Pressure Field. J. Aerosp. Sci., vol. 28, no. 6, June 1961, pp. 457-470.

5. LeBel, Peter J.; and Russell, James M., III: Development of Sensors to Obtain In-Flight Ablation Measurements of Thermal-Protection Materials. NASA TN D-3686, 1966.

6. Belotserkovskii, O. M.: Flow Past a Circular Cylinder With a Detached Shock Wave. RAD 9-TM-59-66 (Contract No. AF04(647)-305), AVCO Corp., Sept. 30, 1959.

7. Wells, P. B.: A Method for Predicting the Thermal Response of Charring Ablation Materials. Doc. No. D2-23256, Boeing Co., 1964.

8. Exton, Reginald J.: Theory and Operation of a Variable Exposure Photographic Pyrometer Over the Temperature Range 1800° to 3600° F (1255° to 2255° K). NASA TN D-2660, 1965.

9. Midden, Raymond E.; and Cocke, Bennie W., Jr.: Description and Initial Calibration of the Langley 20-Inch Hypersonic Arc-Heated Tunnel. NASA TN D-4653, 1968.

TABLE I.- SUMMARY OF SINGULARITY DESIGN

(a) Leeward compression pad and windward umbilical cavity

Spacecraft	Length, l		Width, w		Depth, h		Boundary-layer thickness, δ		δ/h	l/h	Boundary-layer type
	in.	cm	in.	cm	in.	cm	in.	cm			
Leeward compression pad											
Apollo	6.0	15.25	6.0	15.24	0.72	1.83	0.62	1.57	0.861	8.34	Turbulent
Pacemaker	2.52	6.40	2.52	6.40	.302	.767	.26	.66	↓	↓	↓
Windward umbilical cavity											
Apollo	9.12	23.2	13.5	34.3	0.82	2.08	0.34	0.86	0.415	11.1	Laminar
Pacemaker	3.00	7.62	4.44	11.28	.27	.686	.26	.66	.963	↓	Turbulent

(b) Leeward ramp-umbilical combination

Spacecraft	Length, l		Width, w		Ramp height, h_1		Umbilical height, h_2		Boundary-layer thickness, δ		δ/h_1	l/h_1	Boundary-layer type
	in.	cm	in.	cm	in.	cm	in.	cm	in.	cm			
Apollo	11.47	29.10	21.0	53.3	1.78	4.52	3.84	9.75	1.10	2.79	0.618	6.44	Turbulent
Pacemaker	2.71	6.88	3.0	7.62	.42	1.07	.906	2.296	.26	.66	↓	↓	↓

TABLE II.- COMPOSITION OF TEST MATERIALS

Material	Resin	Fiber	Filler	Reinforcement	Specific gravity
Apollo ablator (honeycomb)	Epoxy-novolac	Silicon dioxide	Phenolic microballoons	Honeycomb	0.513
Apollo ablator (molded)	↓	↓	↓	None	.625
Compression-pad material	Phenolic	Glass fabric	None	↓	1.875
Windward-umbilical-cavity material	↓	Glass ↓	↓	↓	2.020

TABLE III.- SENSOR LOCATIONS

Sensor no.	Type	Quadrant, deg	Depth		Distance from cone-cylinder separation plane		Angle, deg
			in.	cm	in.	cm	
1	Spring wire	0 to 90	0.031	0.079	5.75	14.60	45
2			.096	.244			
3			.152	.386			
4			.060	.152			
5			.030	.076	6.375	16.192	
6			.080	.203			
7			.054	.137			
8		90 to 180	.053	.135	3.00	7.62	135
9			.100	.254			
10			.030	.076	4.15	10.54	
11			.100	.254			
12			.060	.152			
13			.031	.079	5.15	13.08	
14			.060	.152			
15			.126	.320			
16			.151	.384			
17			.090	.229			
18			.046	.117			
19			.030	.076	6.00	15.24	
20			.104	.264			
21	Light pipe	180 to 270	.031	.079	6.27	15.93	225
22			.051	.130			
23			.069	.175			
24			.121	.307			
25	Spring wire		.090	.229	2.00	5.08	260
26			.060	.152			
27			.030	.076			
28		270 to 360	.104	.264			280
29			.060	.152			
30			.031	.079			
31			.030	.076	3.00	7.62	315
32			.103	.262			
33			.133	.338			
34			.076	.193			
35			.045	.114	4.15	10.54	
36			.060	.152			
37			.095	.241			
38			.059	.150			
39			.030	.076	5.15	13.08	
40			.062	.157			
41			.093	.236			
42			.120	.305			
43			.075	.190			
44			.051	.130			
45			.038	.097	6.00	15.24	
46			.102	.259			
47			.159	.404			
48			.060	.152			

TABLE IV.- THERMOCOUPLE LOCATIONS

Thermocouple no.	Quadrant, deg	Depth		Distance from cone-cylinder separation plane		Angle, deg
		in.	cm	in.	cm	
1	0 to 90	0.650	1.65	6.375	16.192	40
2	↓	.100	.254	4.30	10.92	45
3	↓	.300	.763	↓	↓	↓
4	↓	.500	1.27	↓	↓	↓
5	↓	On substructure		3.55	9.02	↓
6	90 to 180	.650	1.65	4.15	10.54	130
7	↓	On substructure		5.50	13.98	135
8	180 to 270	.650	1.65	5.65	14.35	220
9	↓	.300	.763	4.565	11.60	225
10	↓	.500	1.27	↓	↓	↓
11	↓	On substructure		3.825	9.72	↓
12	270 to 360	On substructure		5.50	13.98	315

TABLE V.- ENVIRONMENT AT SIMULATION*

Spacecraft	Heating rate		Shear stress		Reynolds number	Mach number	Pressure, atm
	$\frac{Btu}{ft^2\text{-sec}}$	$\frac{kW}{m^2}$	$\frac{lb}{ft^2}$	$\frac{N}{m^2}$			
Leeward compression pad							
Apollo	82.3	934.0	2.3	110.0	3.5×10^5	1.045	0.20
Pacemaker	70.9	805.0	7.2	345.0	4.1×10^5	2.83	.129
Windward umbilical cavity							
Apollo	12.0	136.0	0.94	45.0	3.2×10^4	2.60	0.0155
Pacemaker	70.9	805.0	7.2	345.0	4.1×10^5	2.83	.129
Leeward ramp-umbilical combination							
Apollo	75.4	855.0	2.2	105.5	5.5×10^5	1.265	0.15
Pacemaker	70.9	805.0	7.2	345.0	4.1×10^5	2.83	.129

*When the heating rate is a maximum during the second heating period for Apollo and at fourth-stage burnout (85.6 seconds) for Pacemaker.

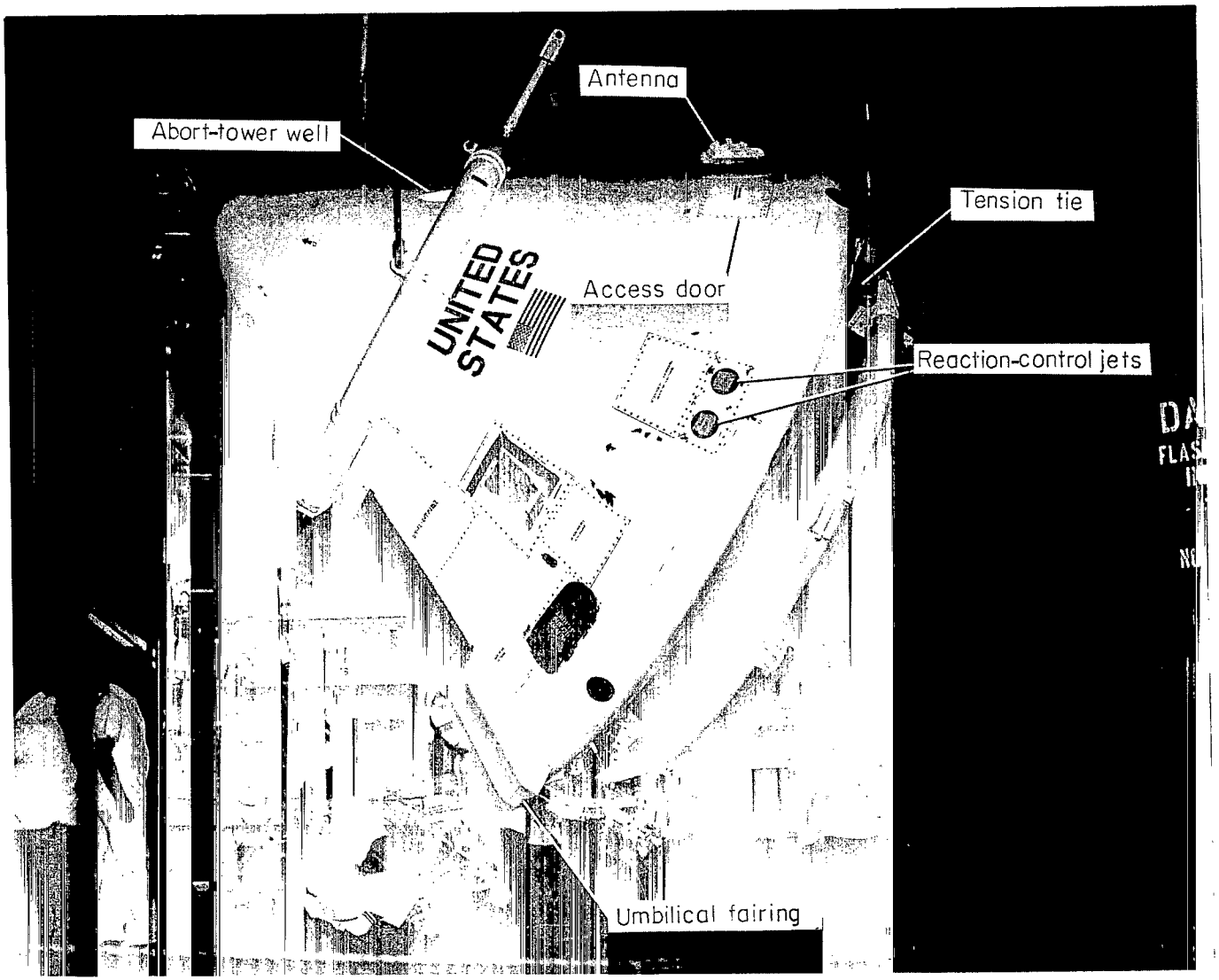

(a) Side view.

L-68-5637

Figure 1.- Photographs of Apollo command module showing heat-shield singularities.

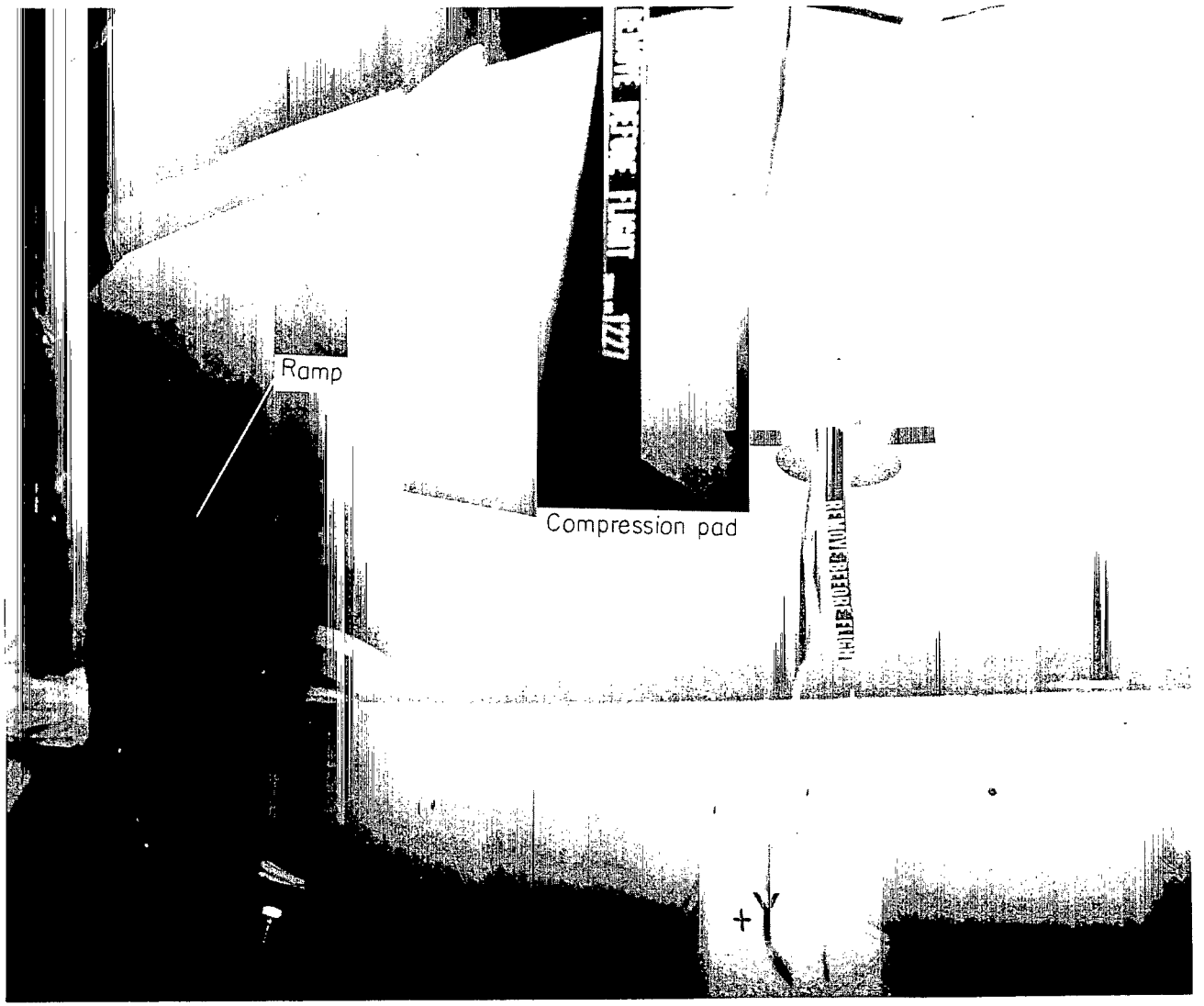

(b) View of forward heat shield.

L-68-5638

Figure 1.- Concluded.

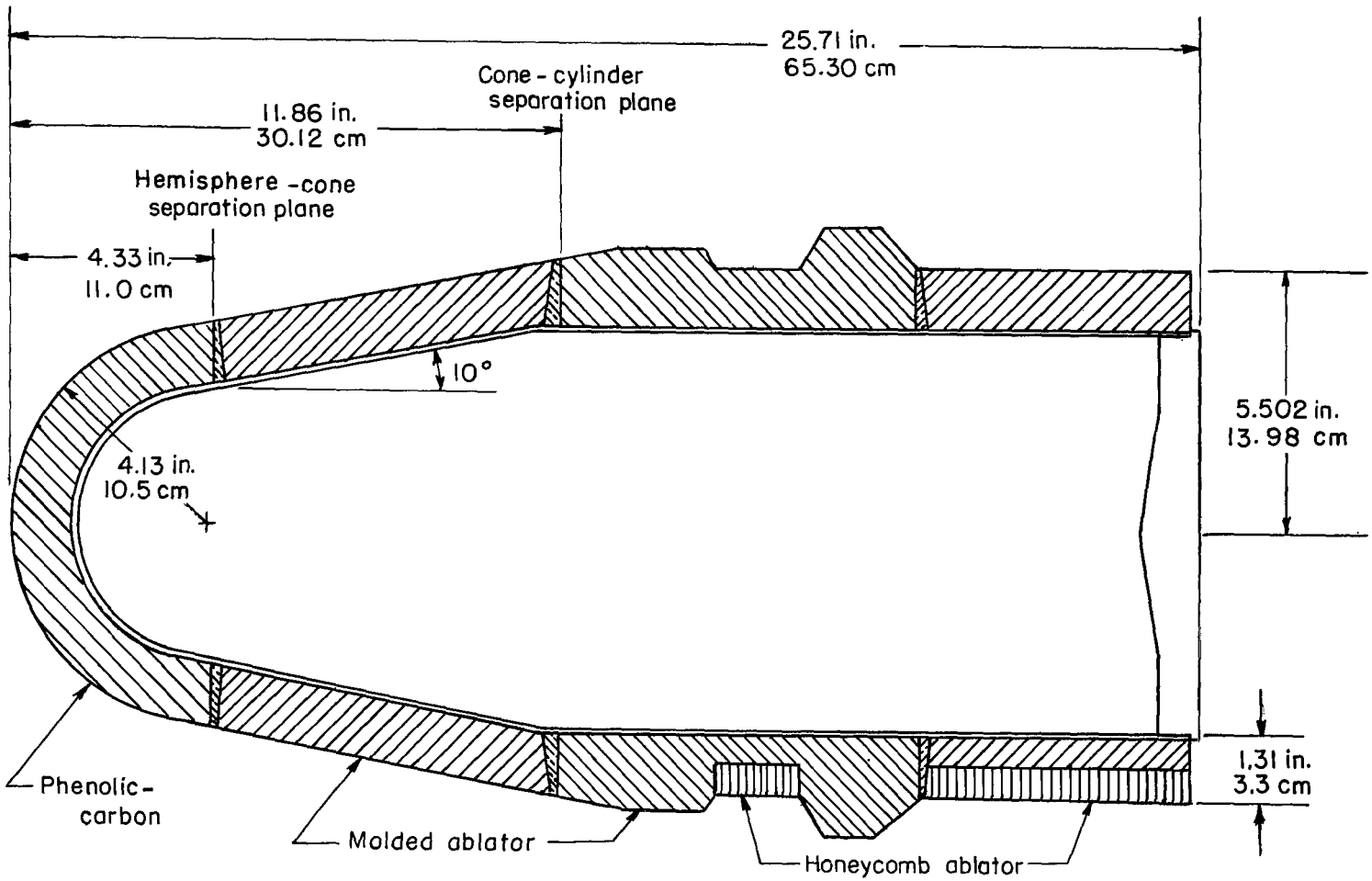

Figure 2.- Sketch of the Pacemaker spacecraft.

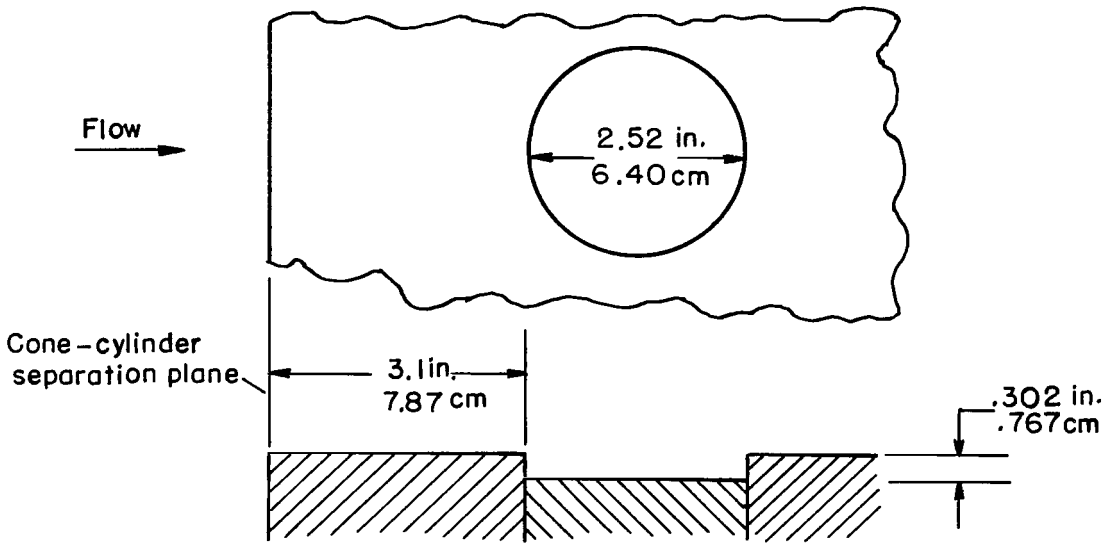

(a) Leeward compression pad.

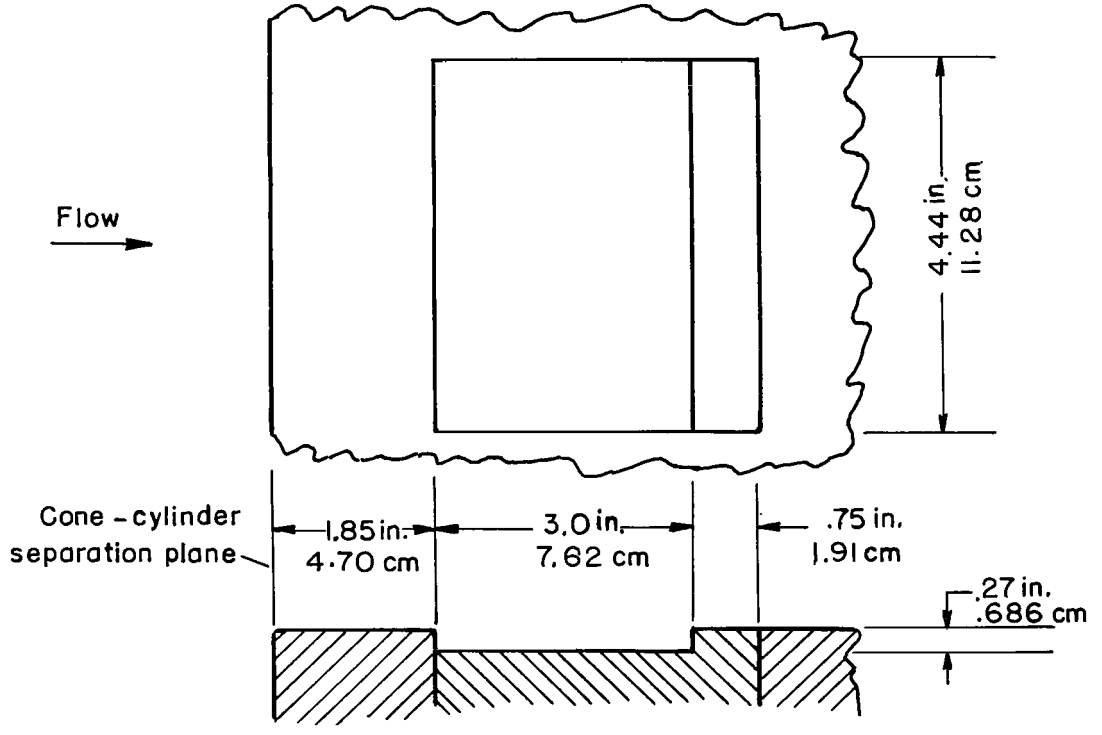

(b) Windward umbilical cavity.

Figure 3.- Sketch of simulated compression pad and windward umbilical cavity.

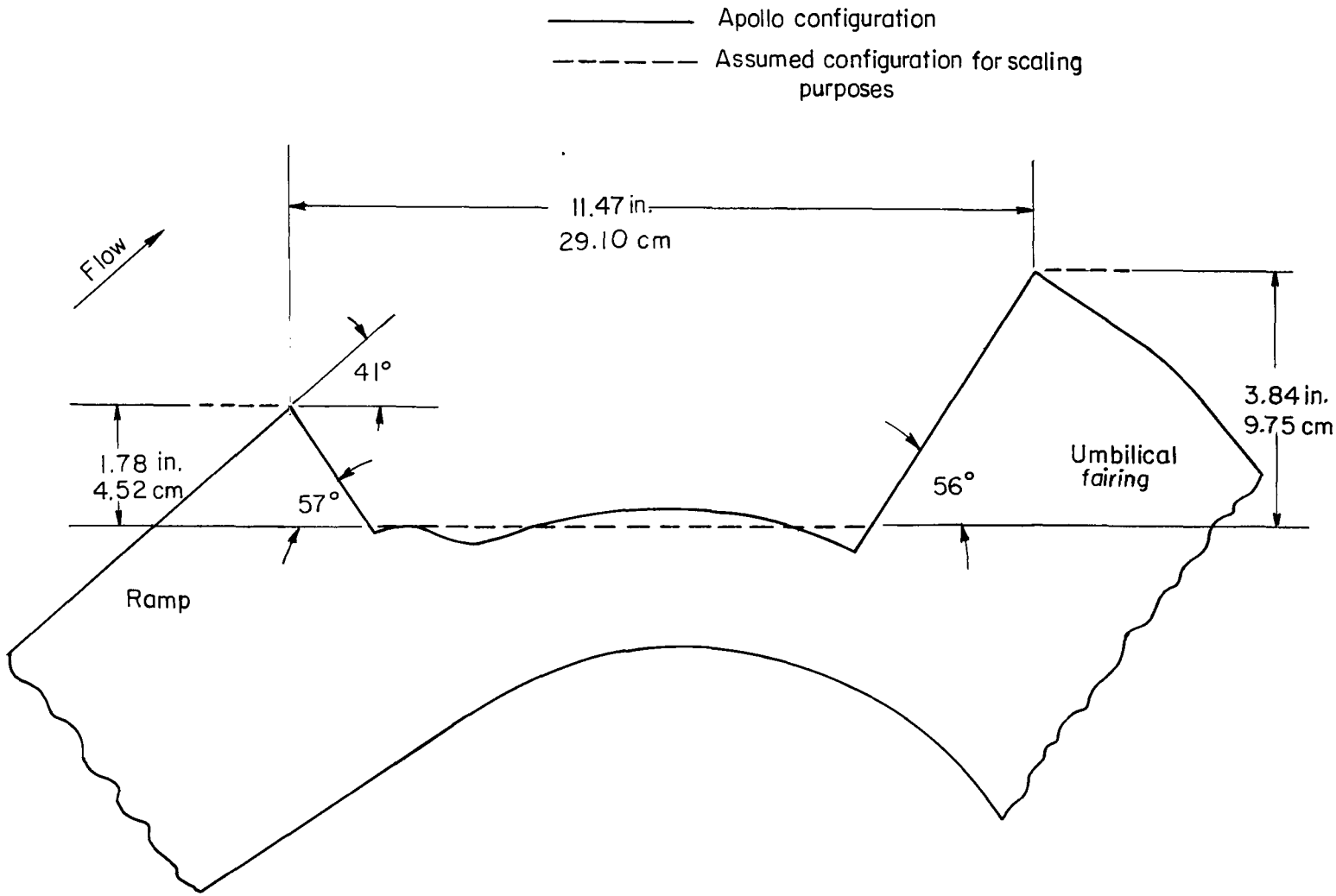

Figure 4.- Apollo ramp-umbilical combination.

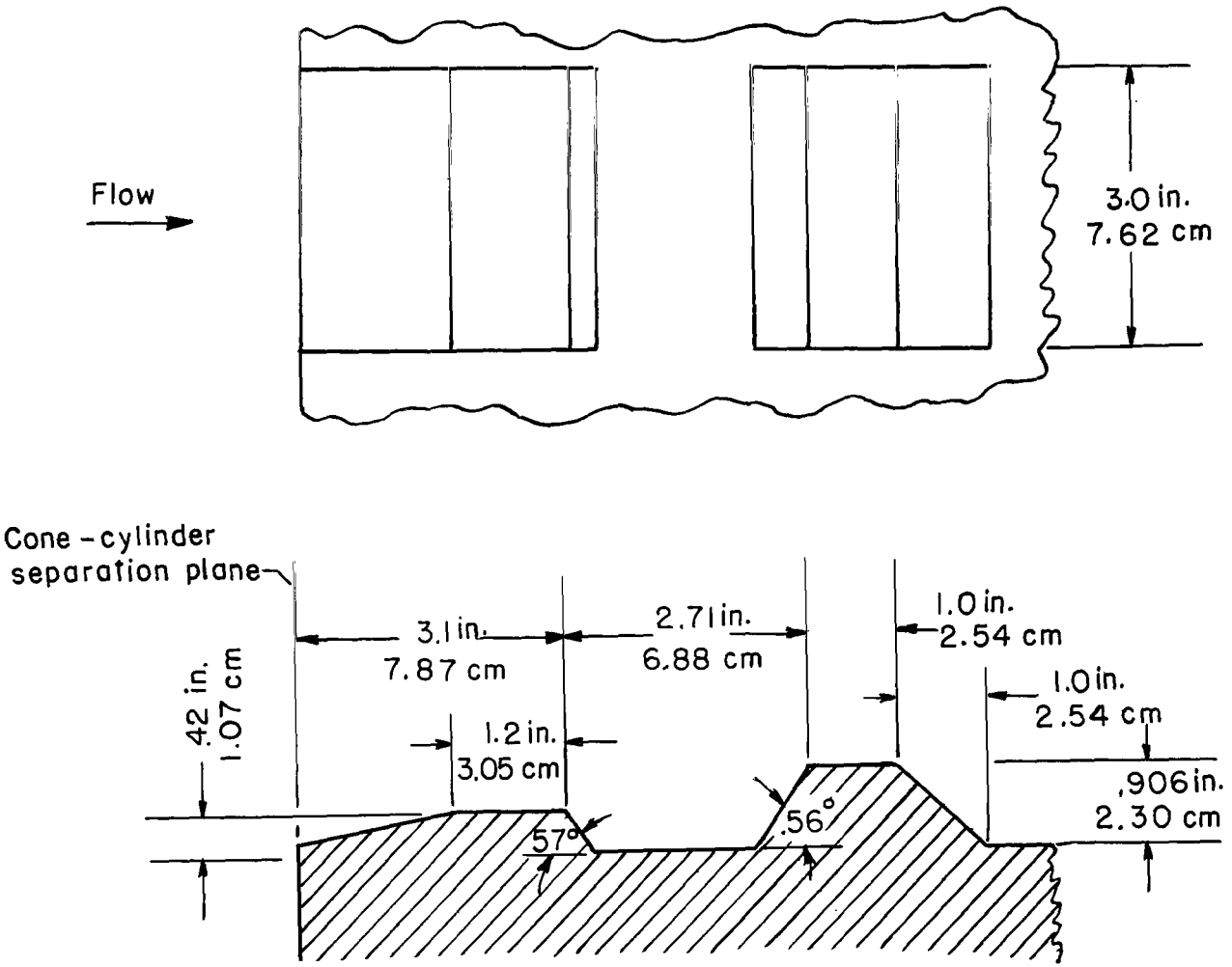

Figure 5.- Sketch of ramp-umbilical simulation on Pacemaker spacecraft.

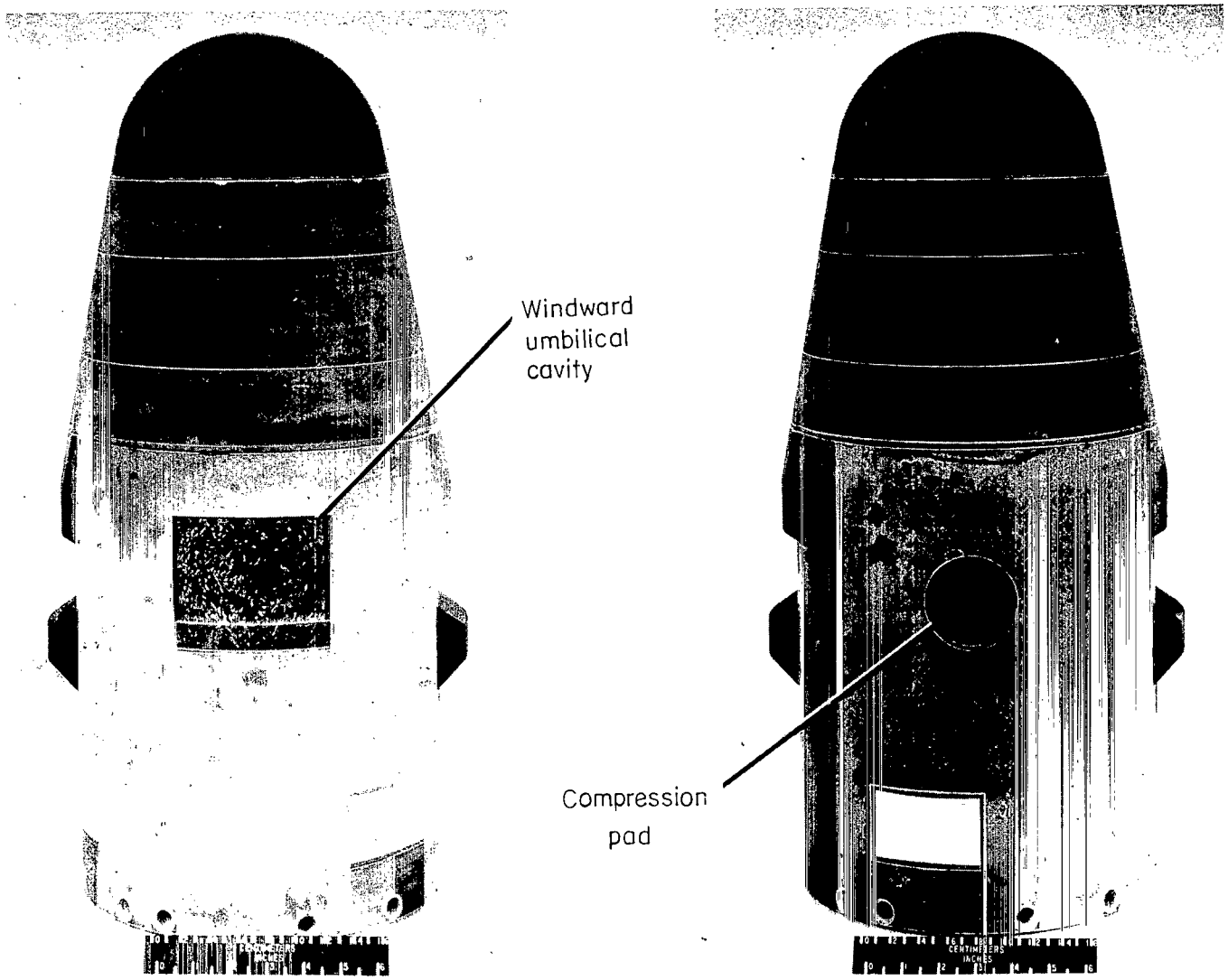

(a) View of windward umbilical cavity.

(b) View of compression pad.

L-68-5639

Figure 6.- Photographs of Pacemaker spacecraft showing simulated singularities.

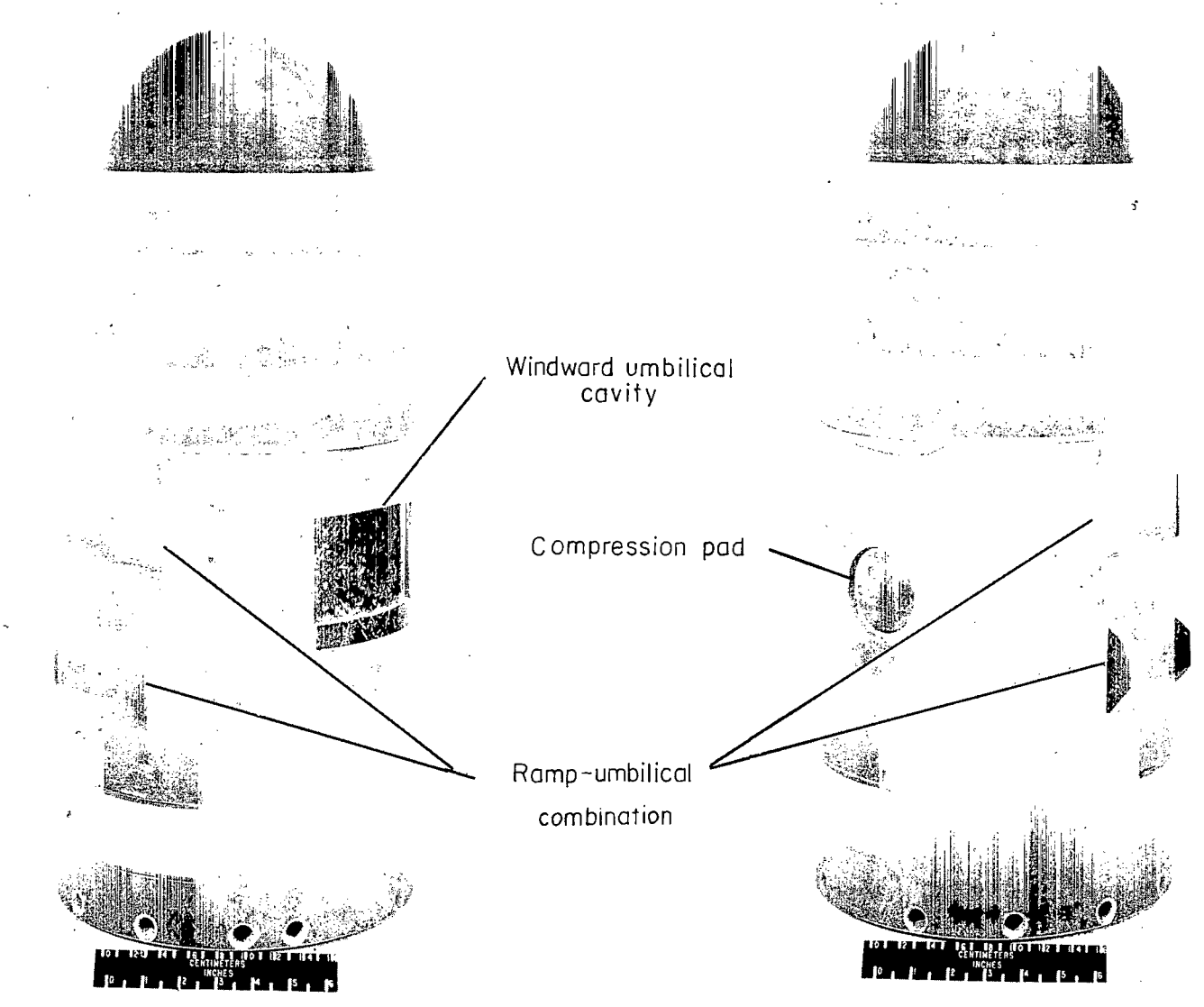

(c) View of ramp-umbilical combination and windward umbilical cavity. L-66-7388.1

(d) View of compression pad and ramp-umbilical combination. L-66-7387.1

Figure 6.- Concluded.

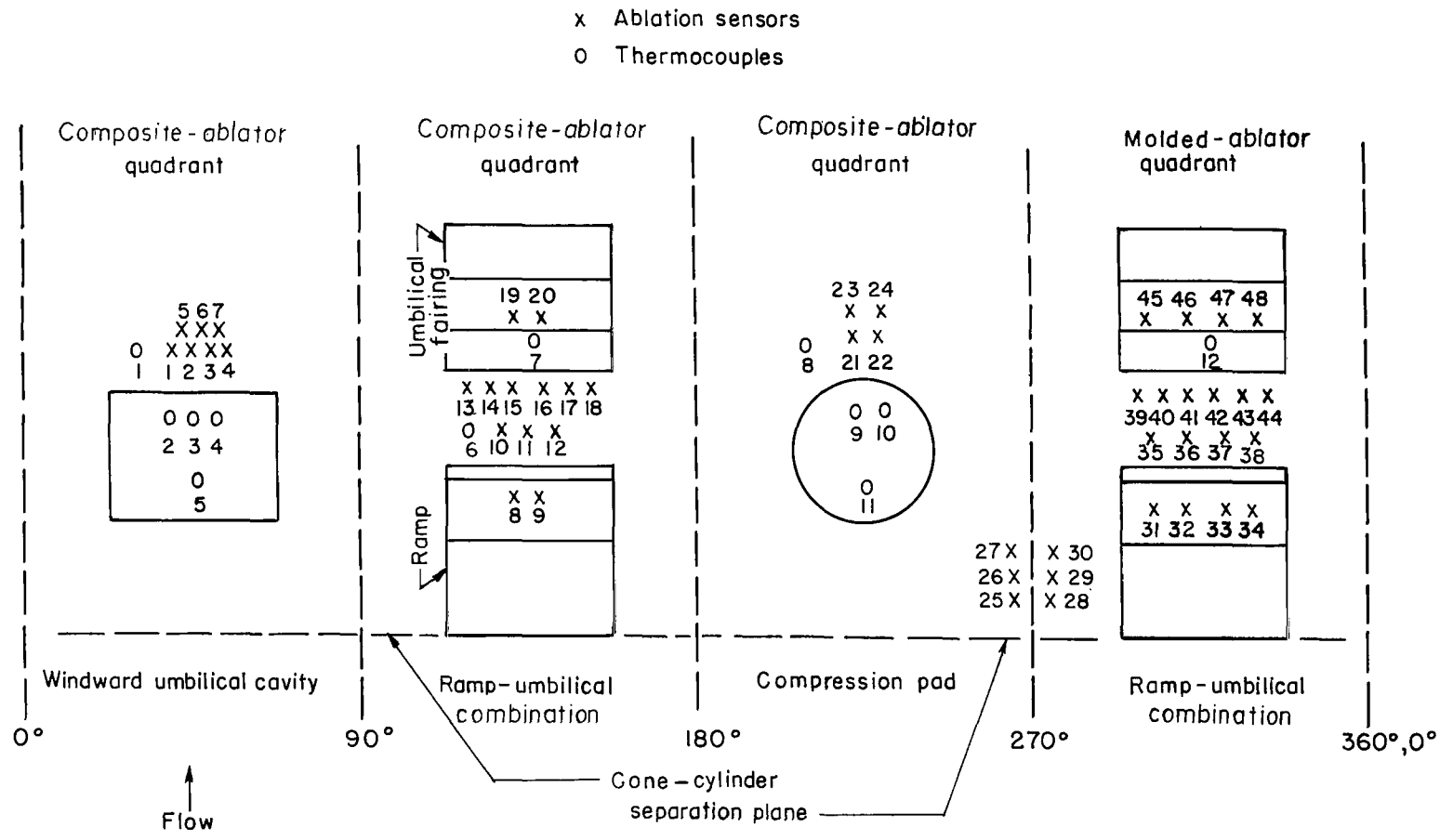

Figure 7.- Schematic diagram of singularities showing location of instrumentation.

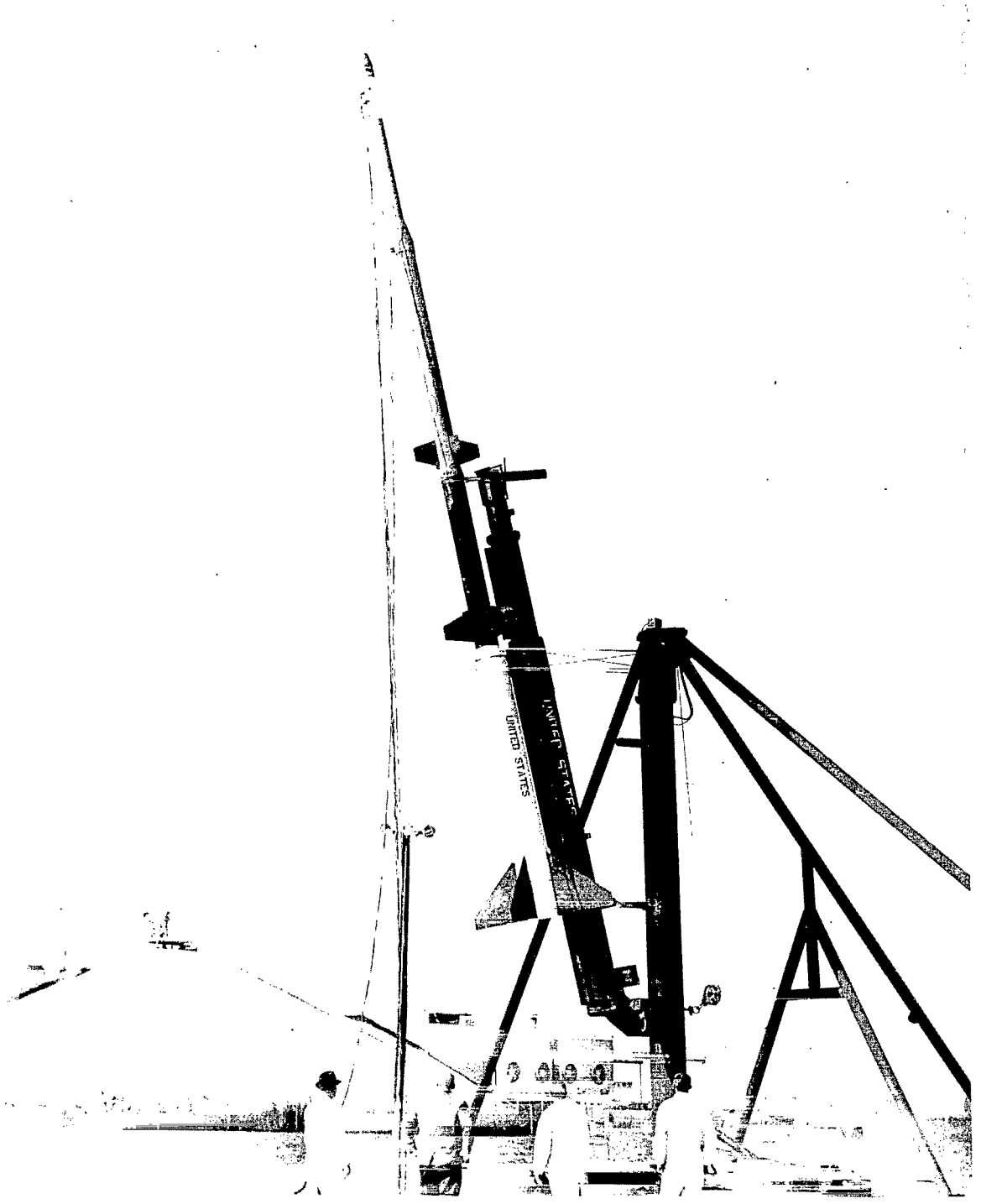

Figure 8.- Photograph of spacecraft and Pacemaker launch vehicle. L-66-590

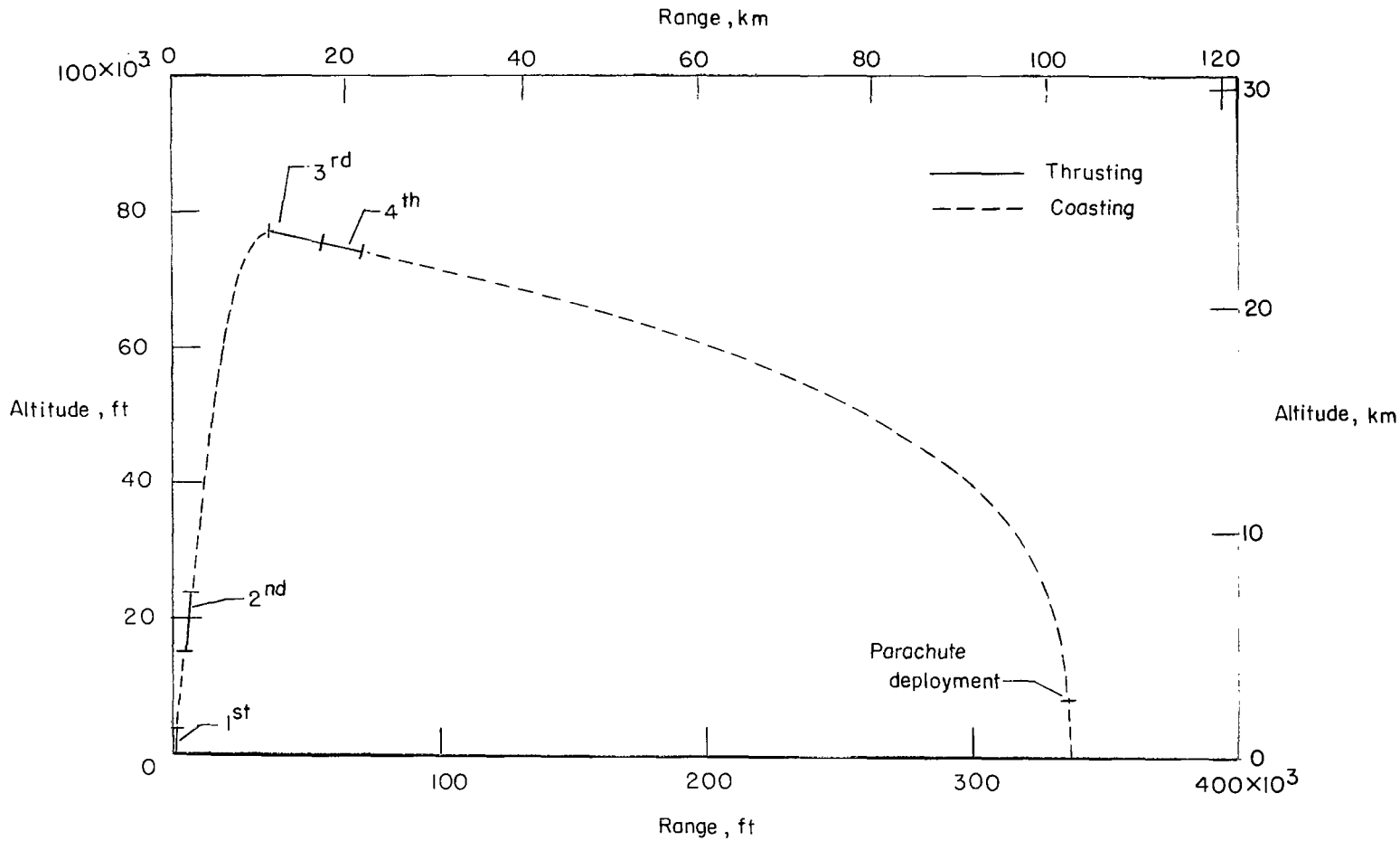

Figure 9.- Flight trajectory showing sequence of events.

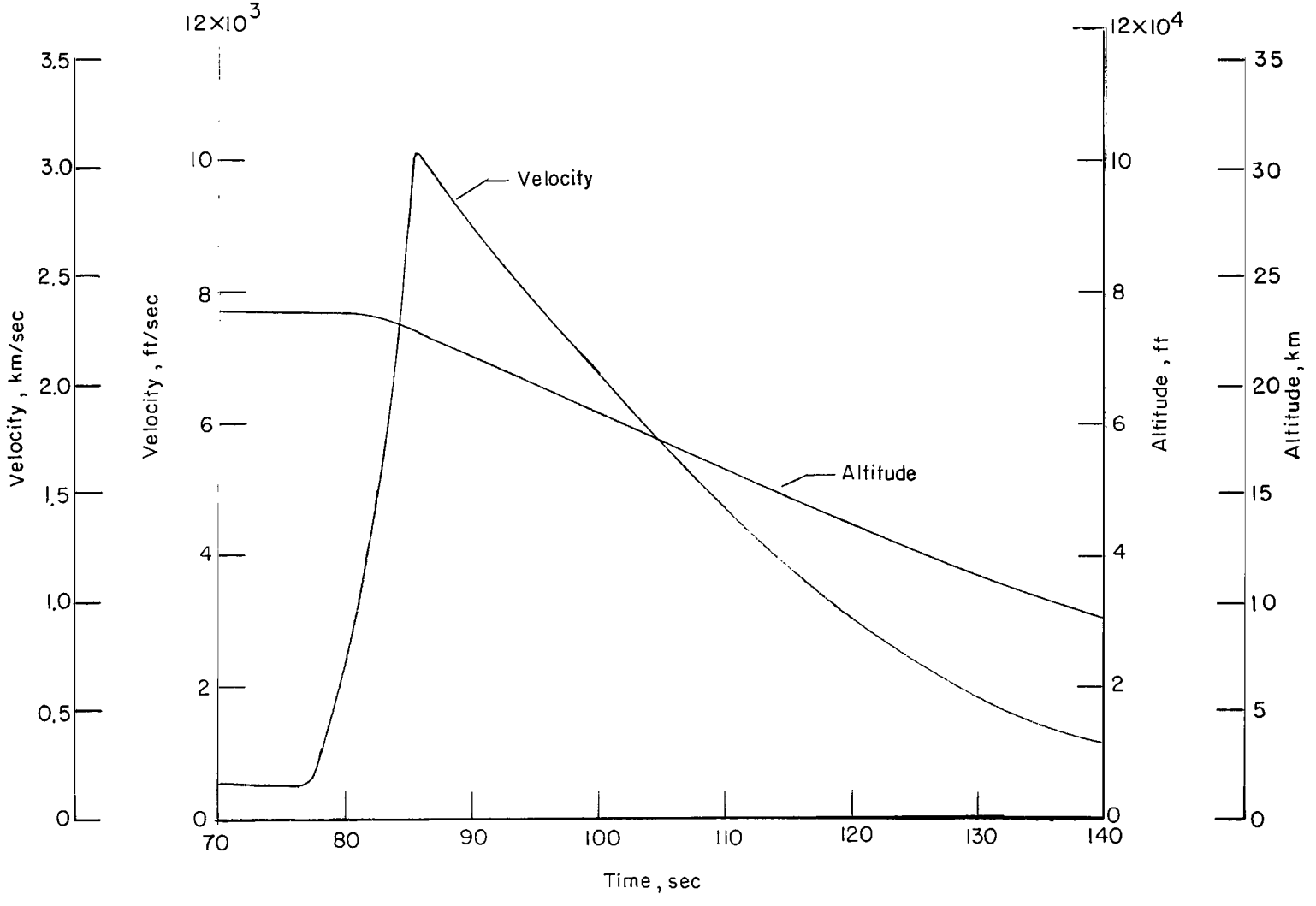

Figure 10.- Time history of velocity and altitude during data period.

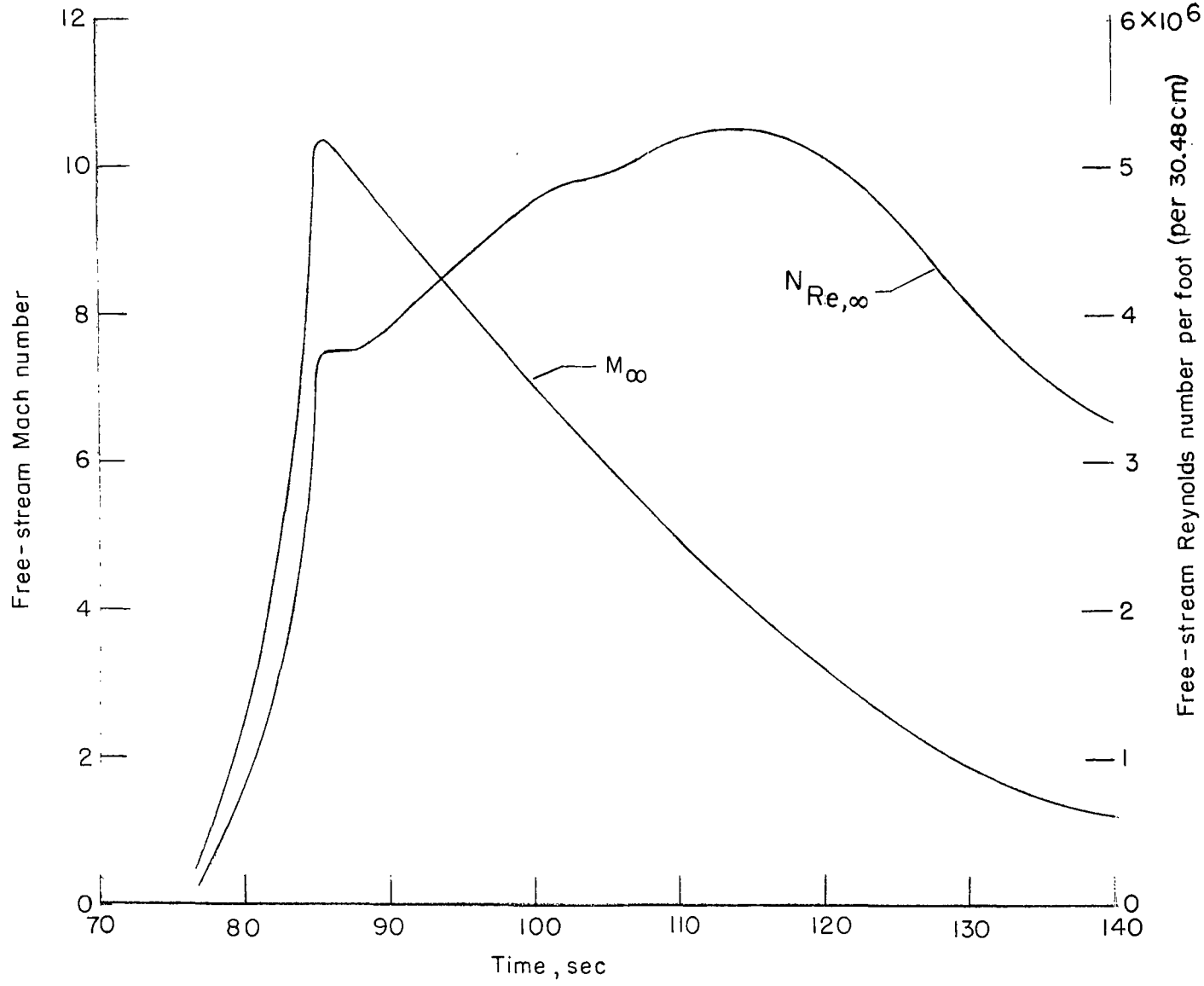

Figure 11.- Time history of Mach number and Reynolds number during data period.

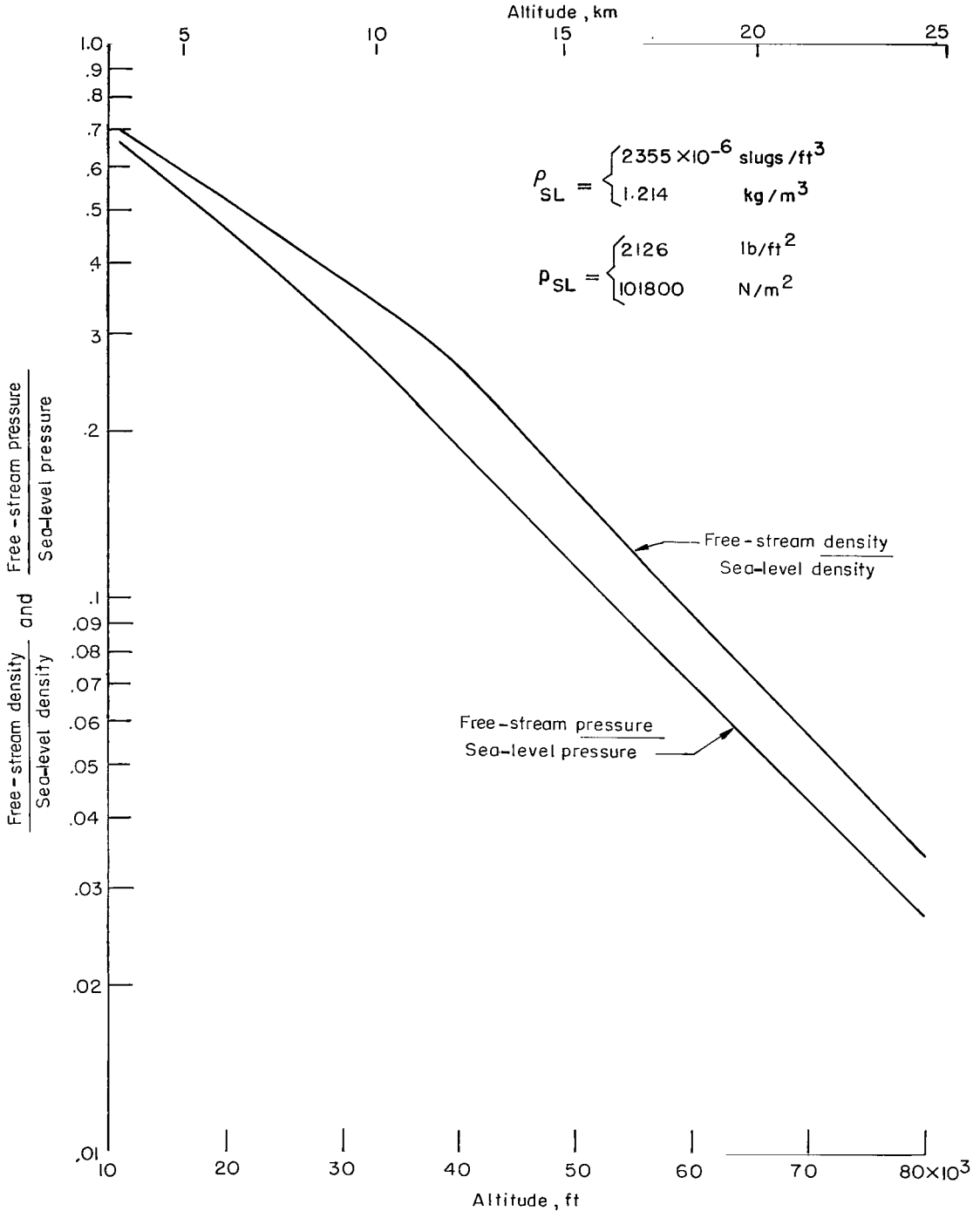

(a) Nondimensional pressure and density variation with altitude.

Figure 12.- Atmospheric data.

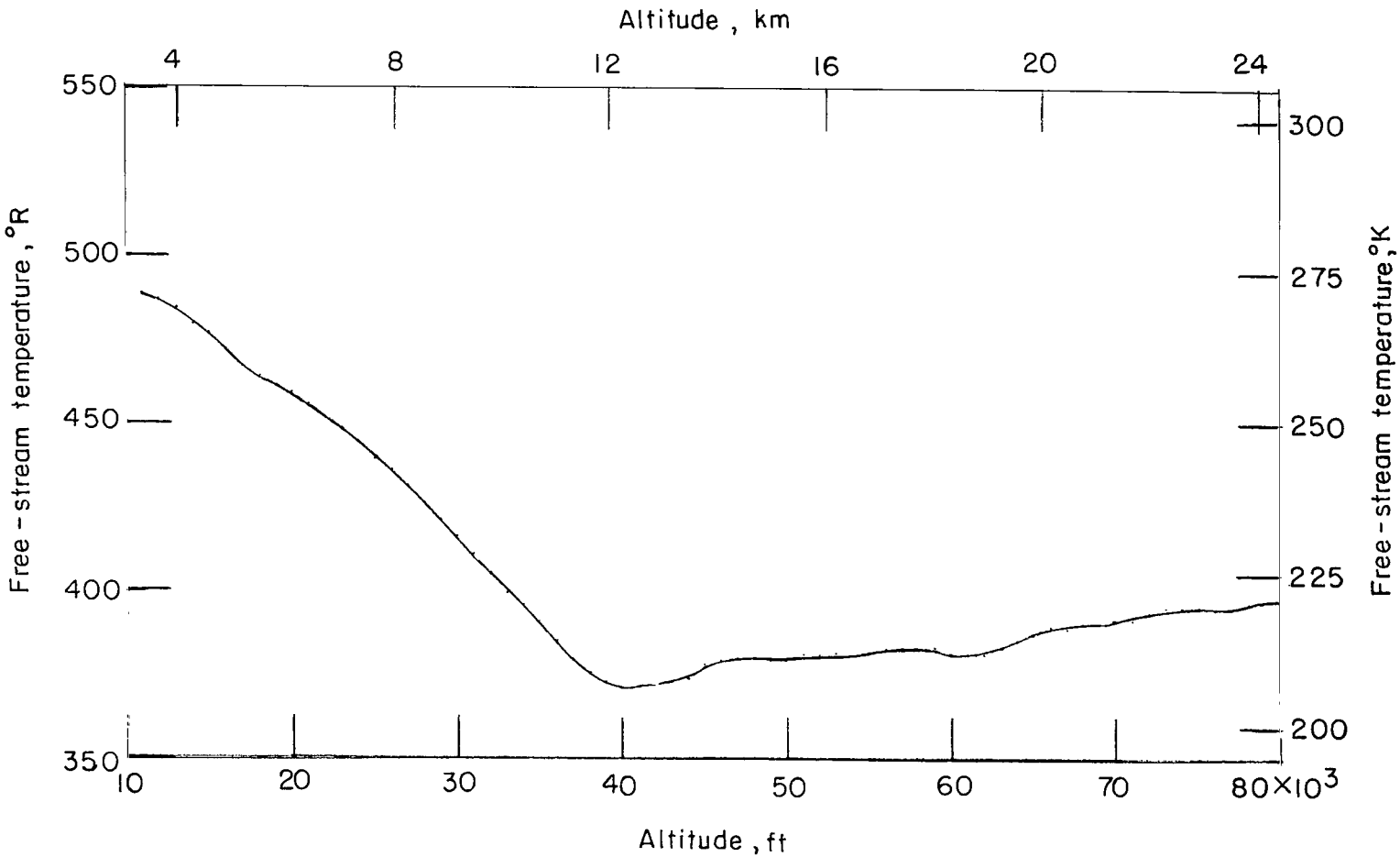

(b) Temperature variation with altitude.

Figure 12.- Concluded.

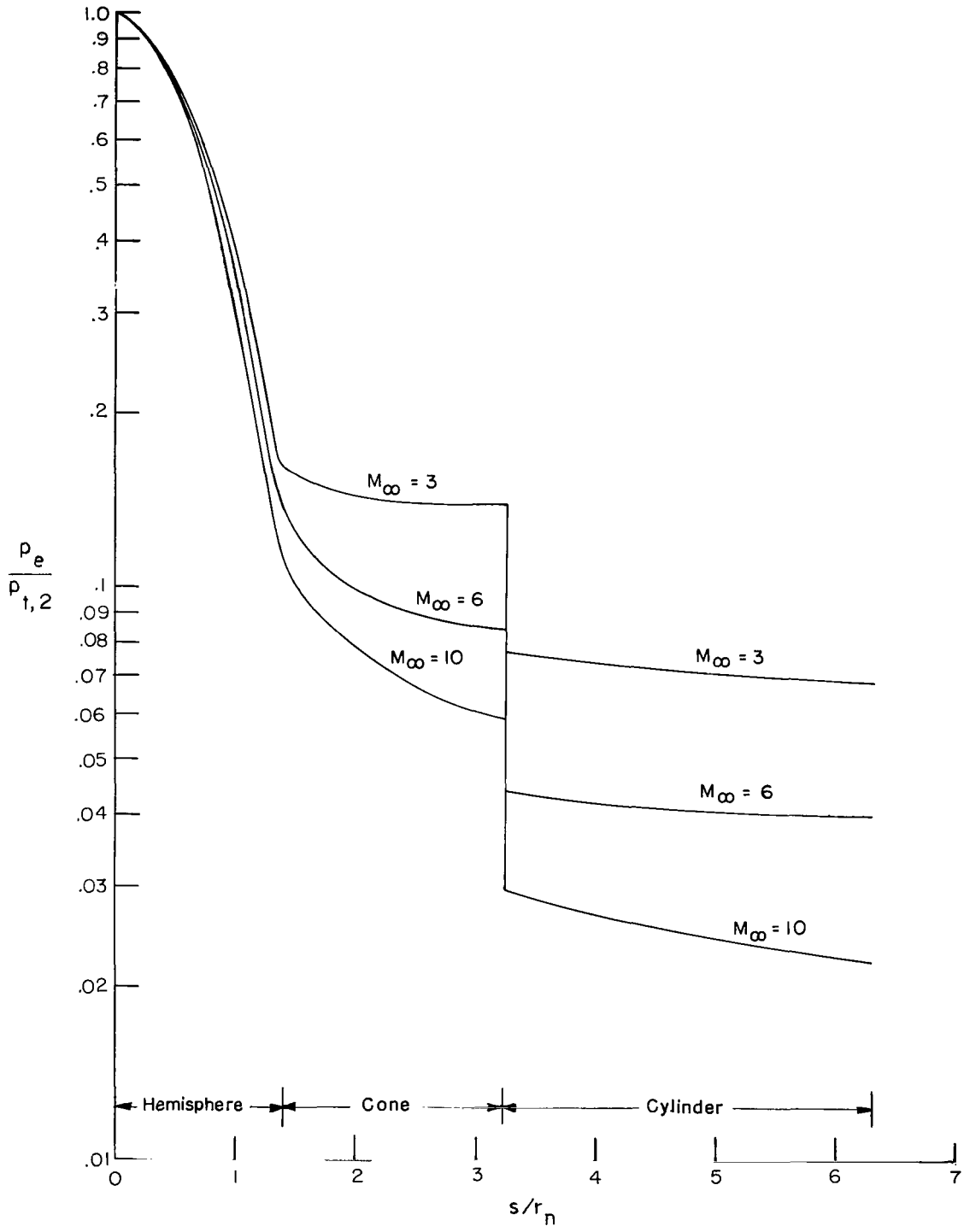

Figure 13.- Pressure distributions over the spacecraft.

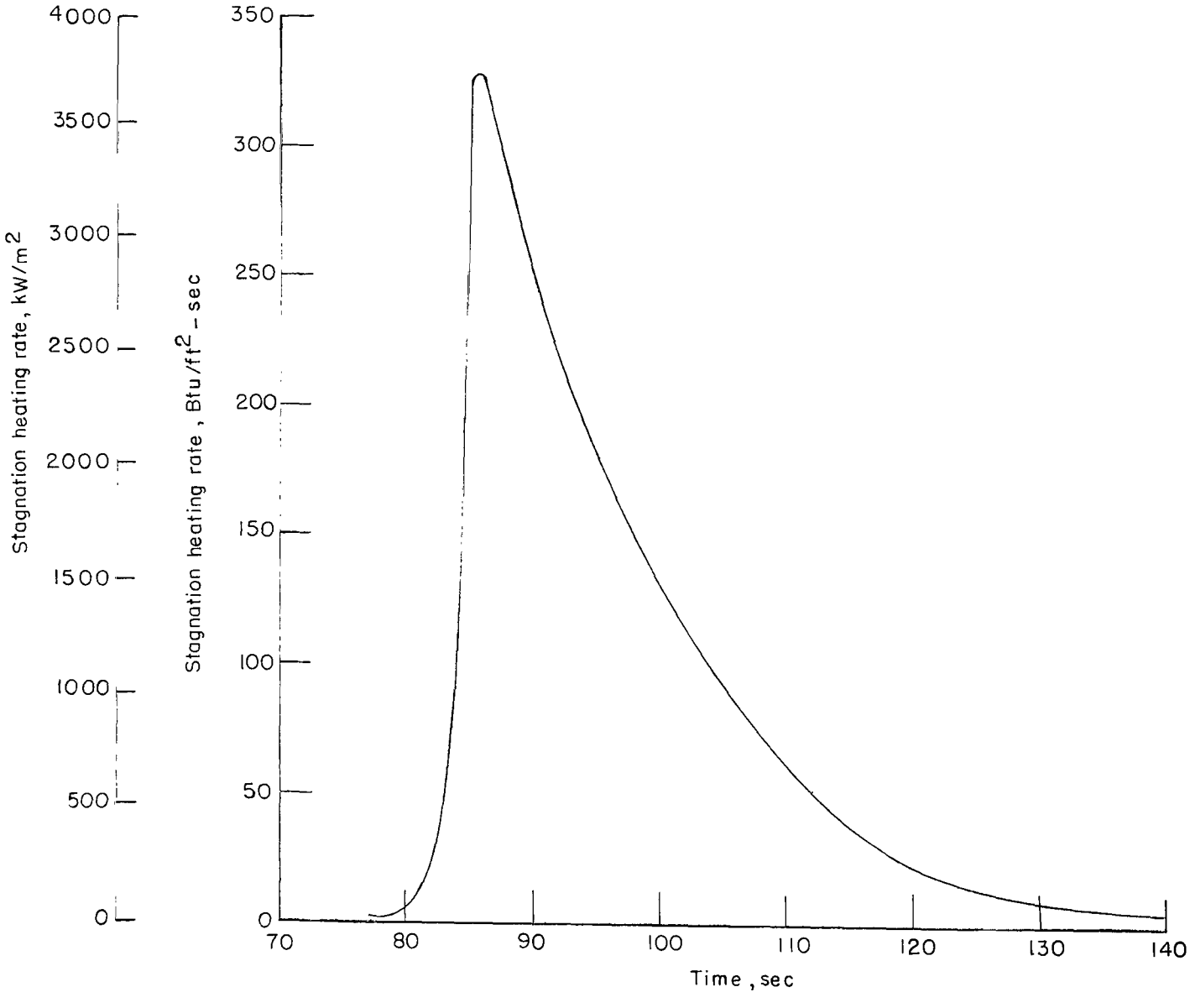

Figure 14.- Time history of stagnation-point heating rate on Pacemaker nose during data period.

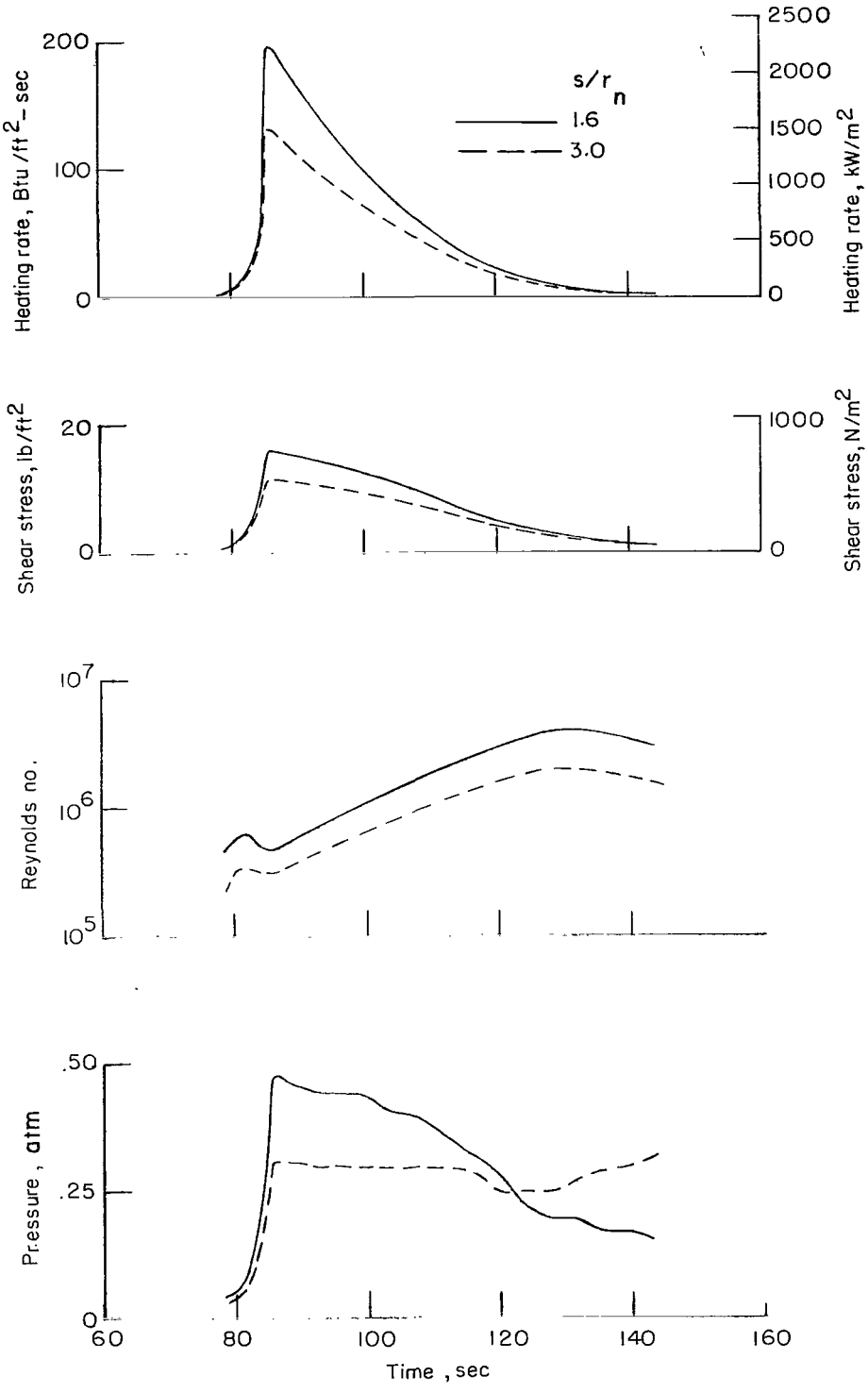

Figure 15.- Time histories of heating rate, shear stress, Reynolds number, and pressure on Pacemaker cone.

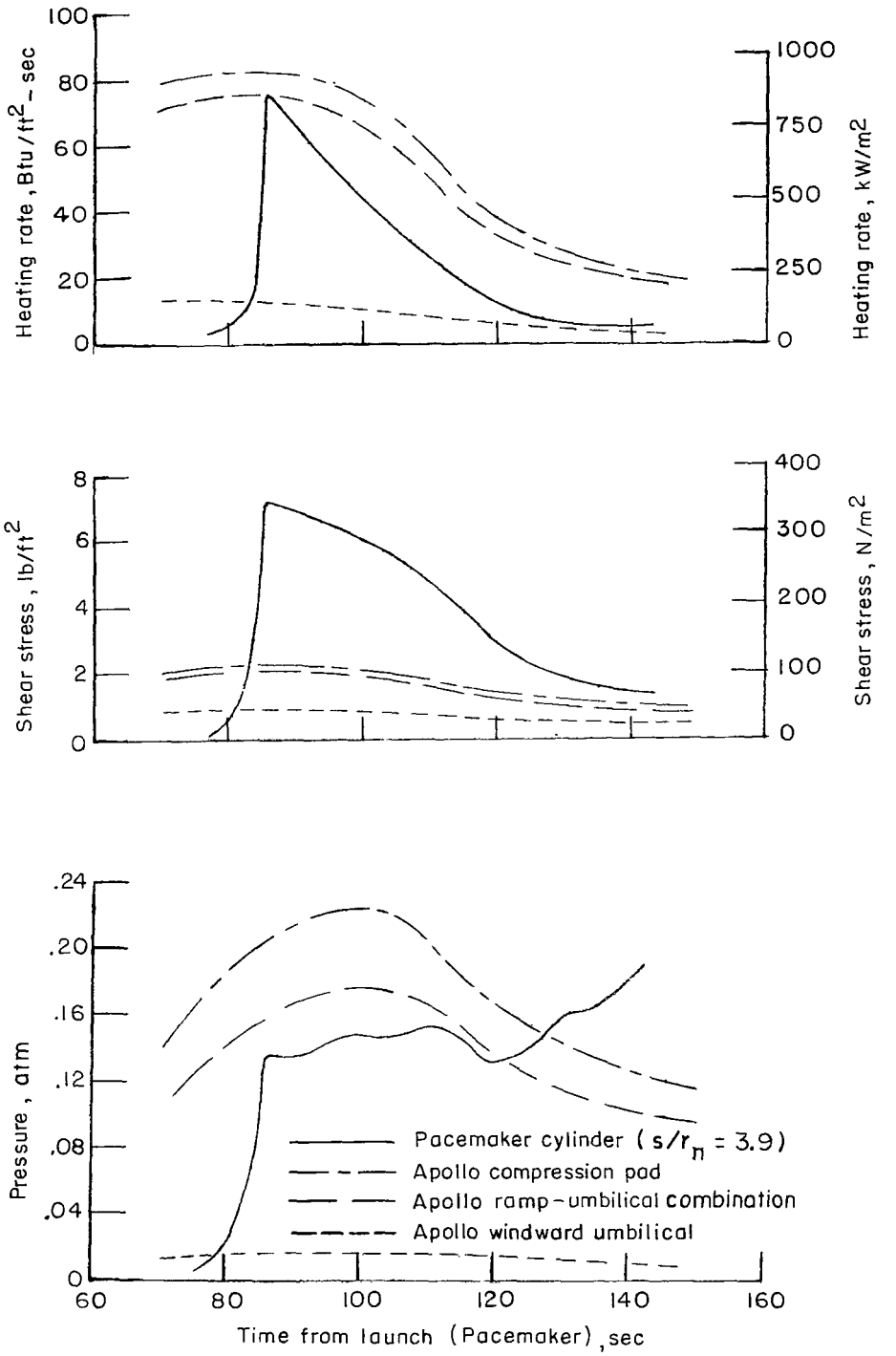

(a) Time histories of heating, shear, and pressure.

Figure 16.- Overlay of Pacemaker and Apollo environment.

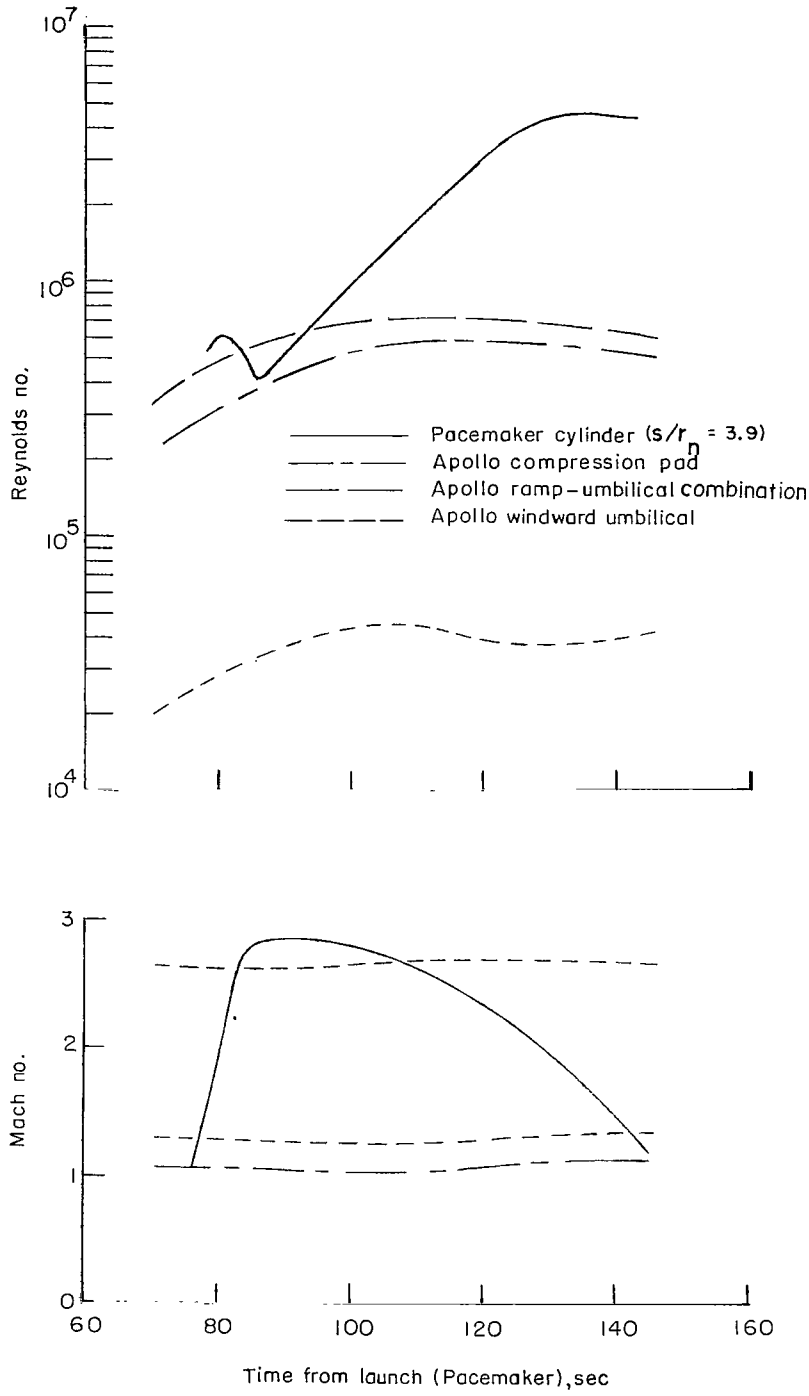

(b) Time histories of Reynolds number and Mach number.

Figure 16.- Concluded.

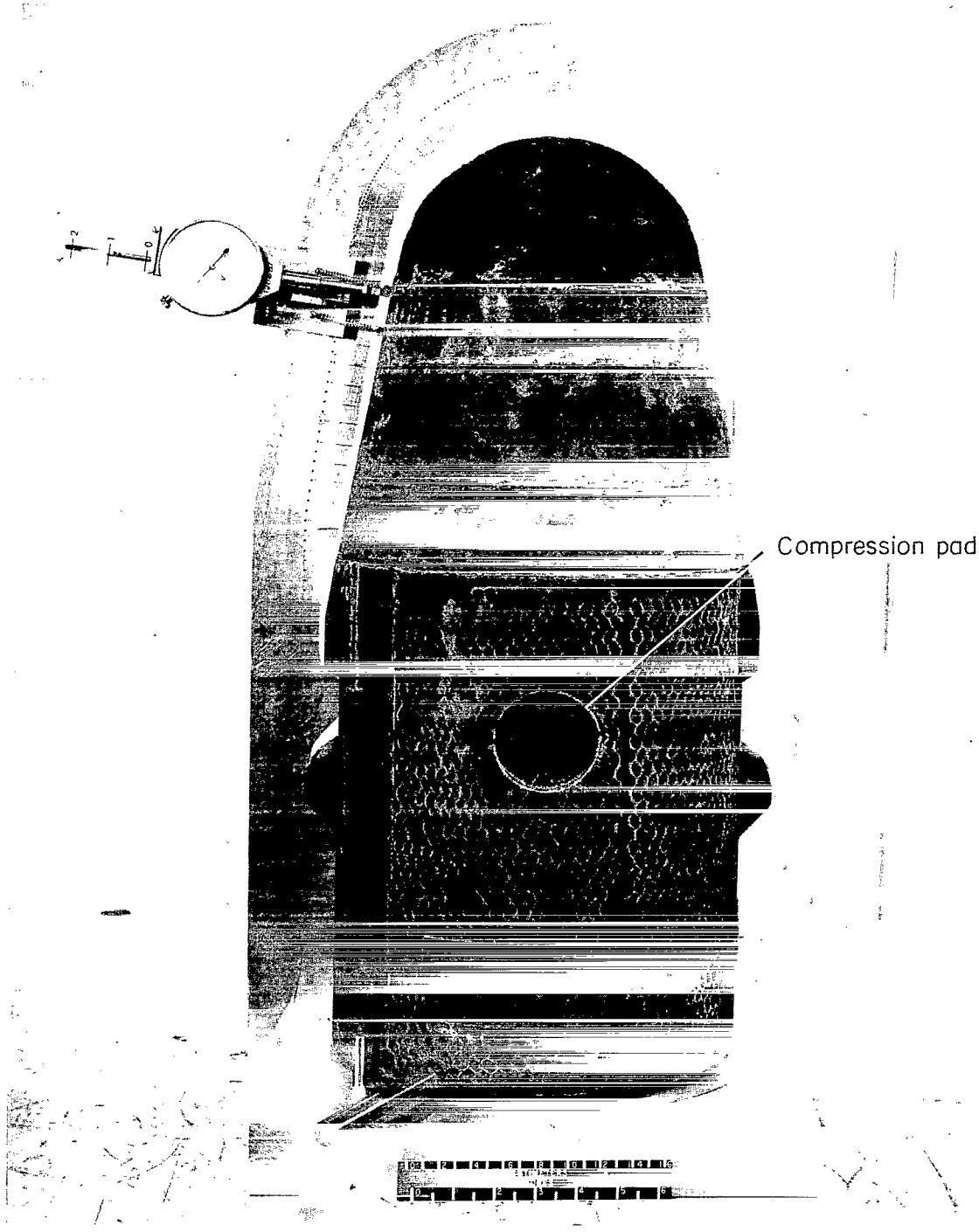

(a) View of compression pad.

L-66-8971.1

Figure 17.- Photographs of the recovered spacecraft.

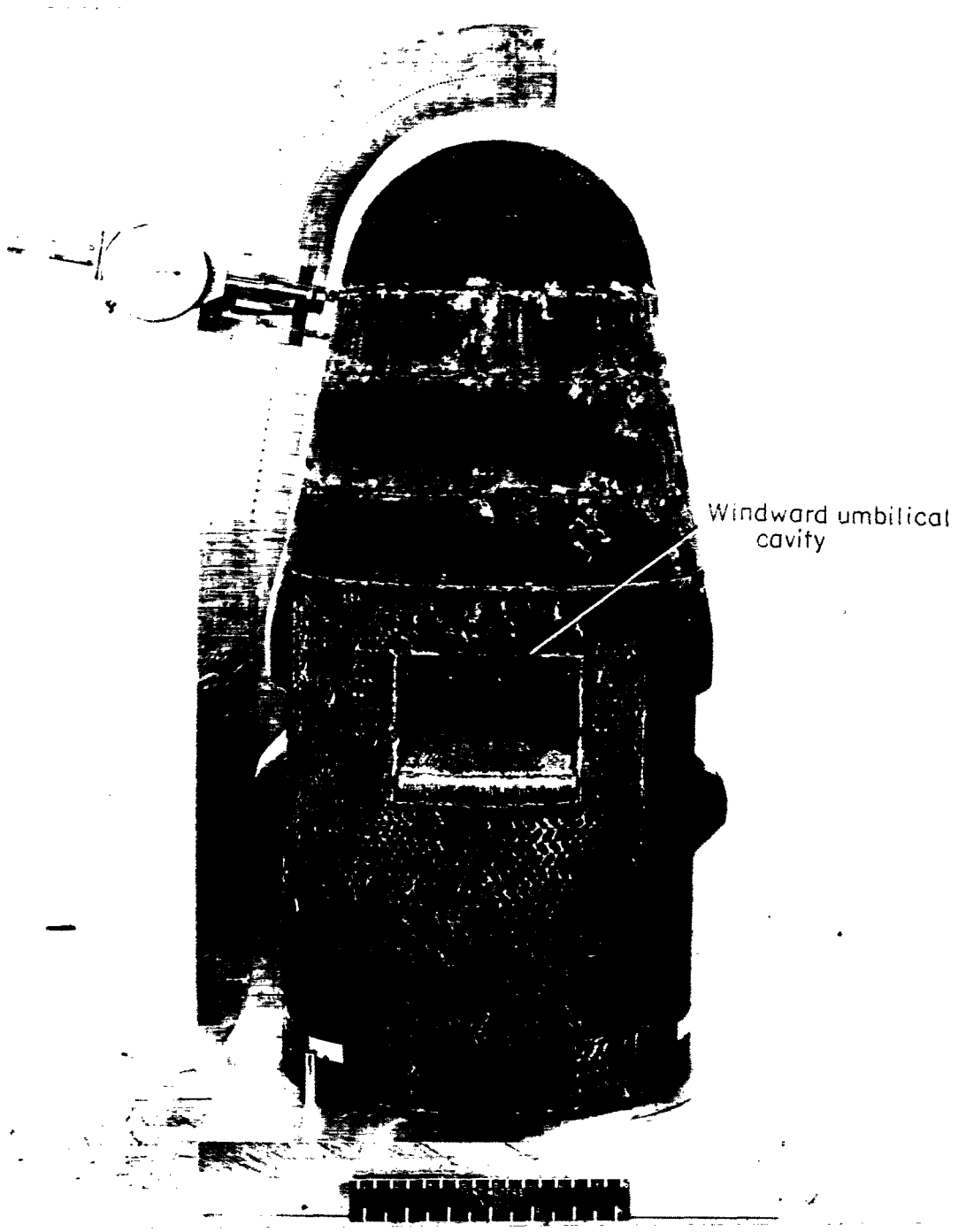

(b) View of windward umbilical cavity. L-66-8968.1

Figure 17.- Continued.

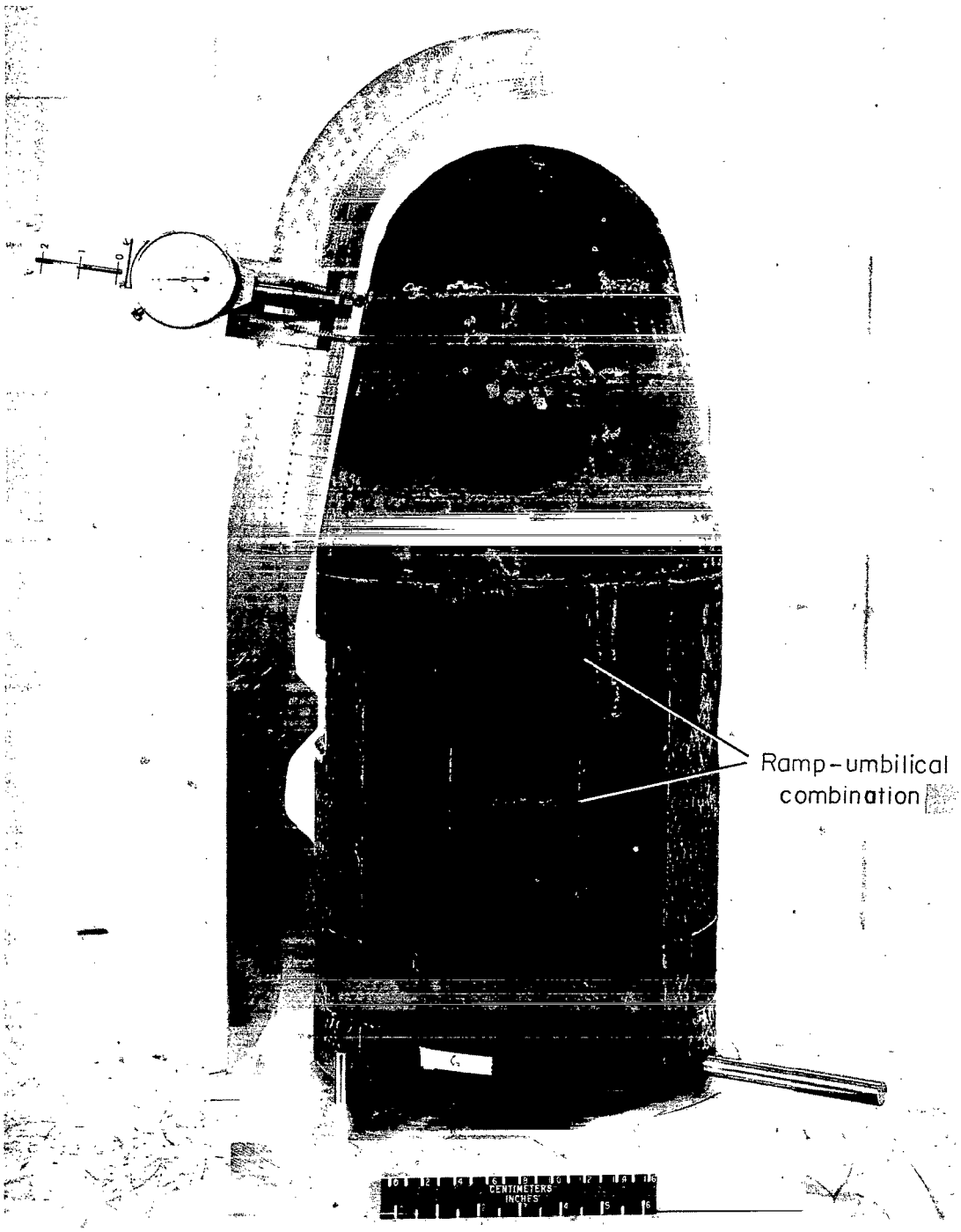

(c) View of ramp-umbilical combination in molded-ablator quadrant. L-66-8970.1

Figure 17.- Continued.

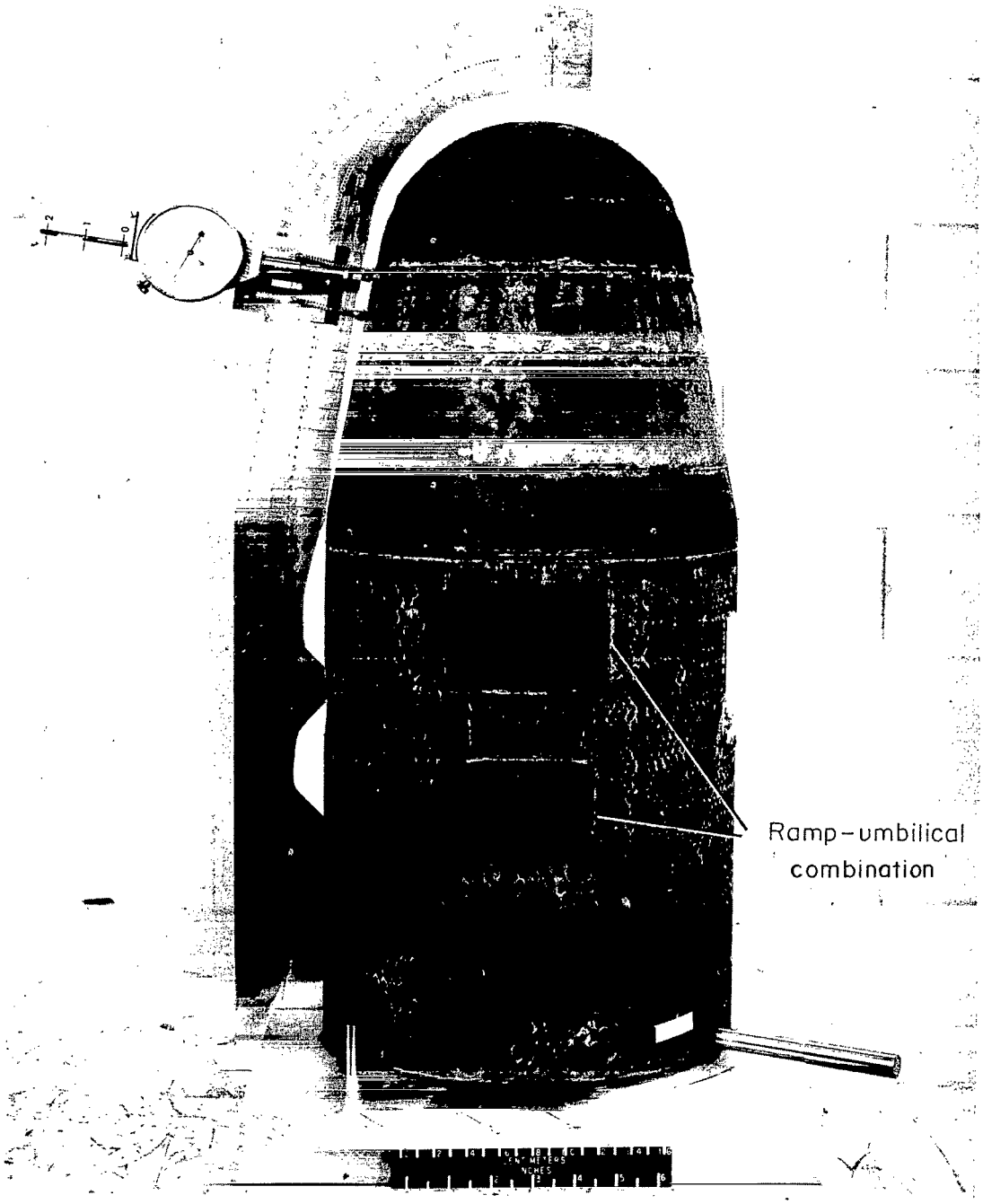

(d) View of ramp-umbilical combination in composite-ablator quadrant. L-66-8972.1

Figure 17.- Concluded.

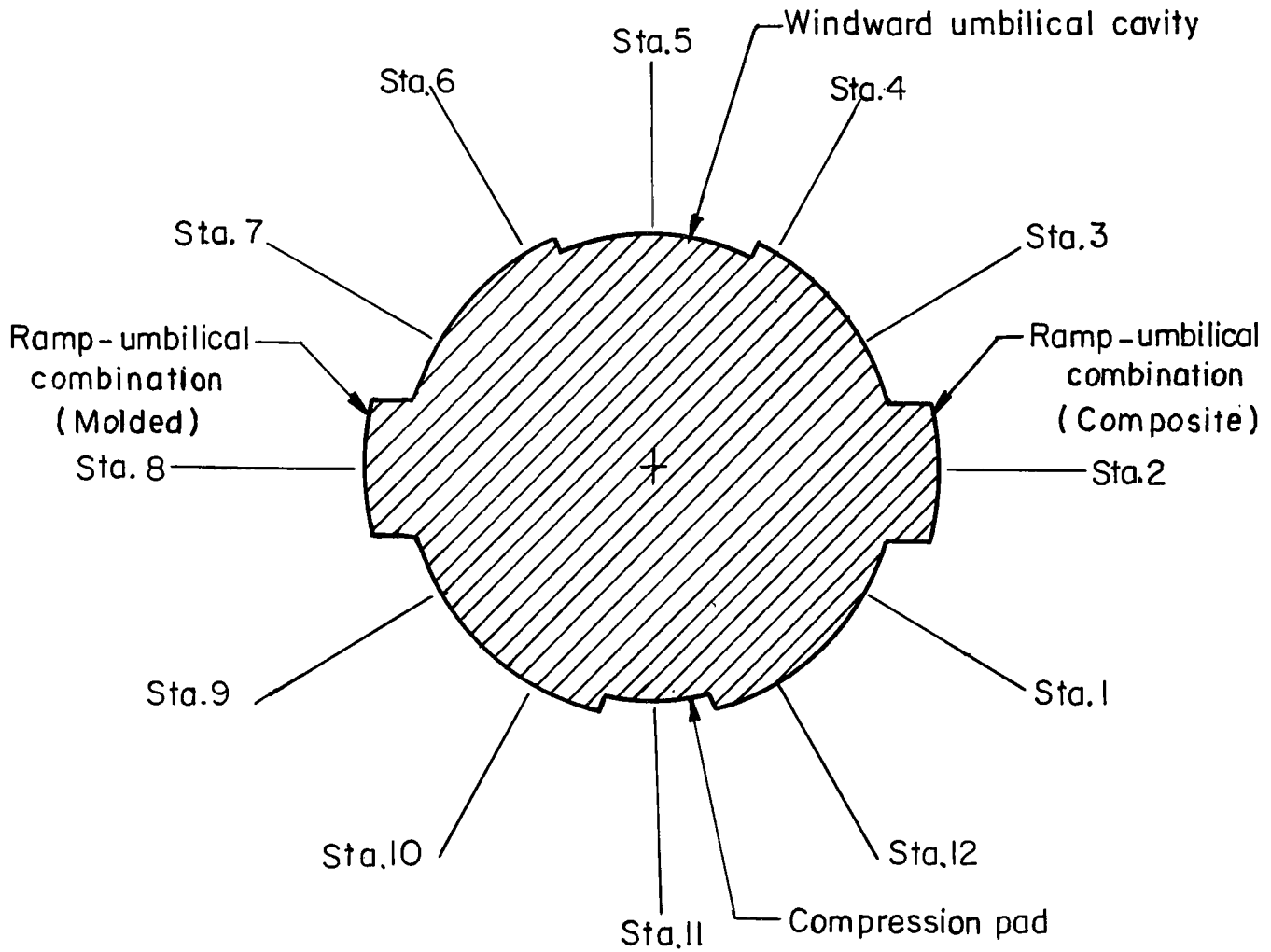

Figure 18.- Sketch showing measurement stations around periphery of spacecraft.

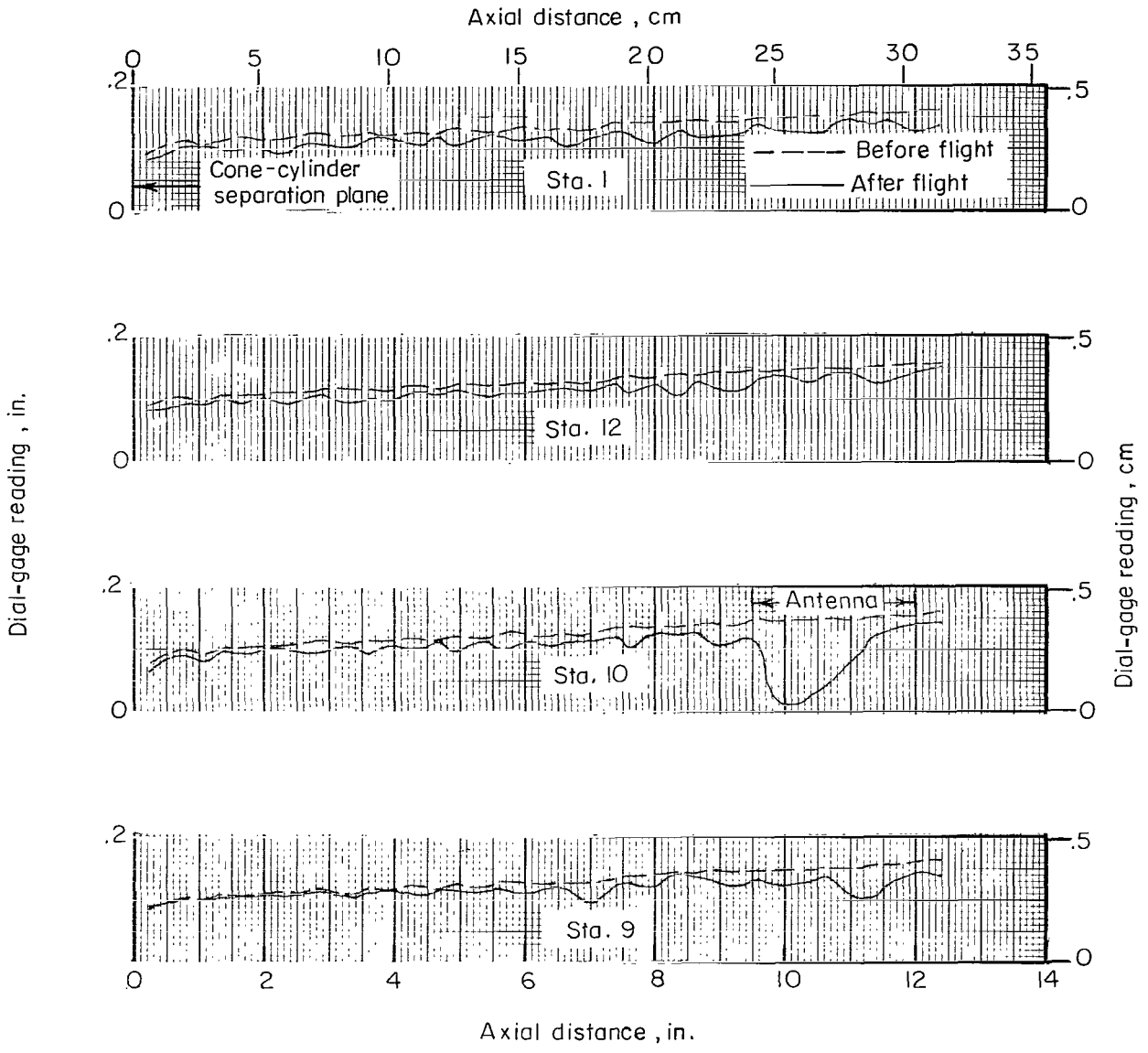

(a) Stations 1, 12, 10, and 9.

Figure 19.- Surface recession experienced by spacecraft along cylindrical section.

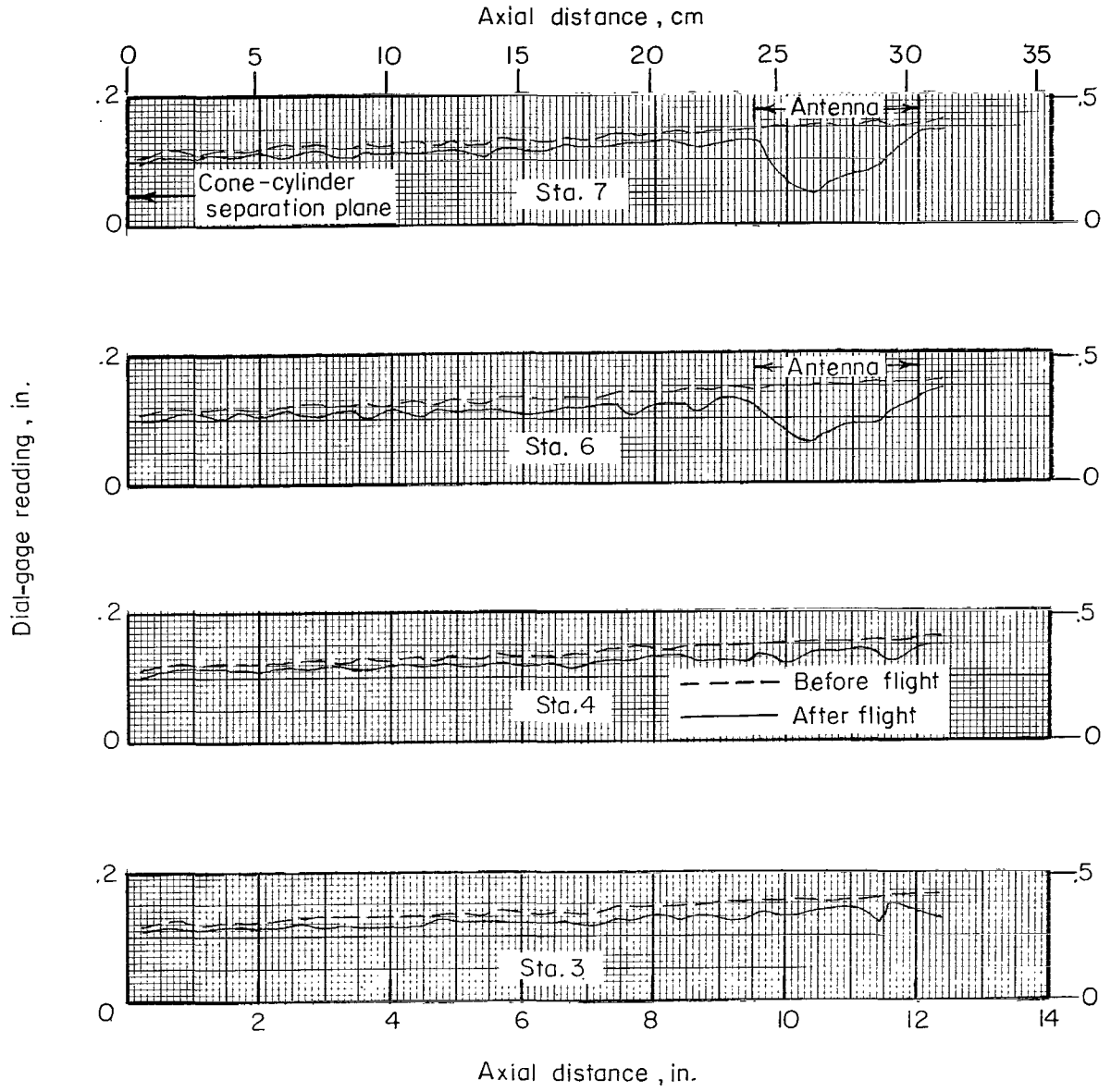

(b) Stations 7, 6, 4, and 3.

Figure 19.- Continued.

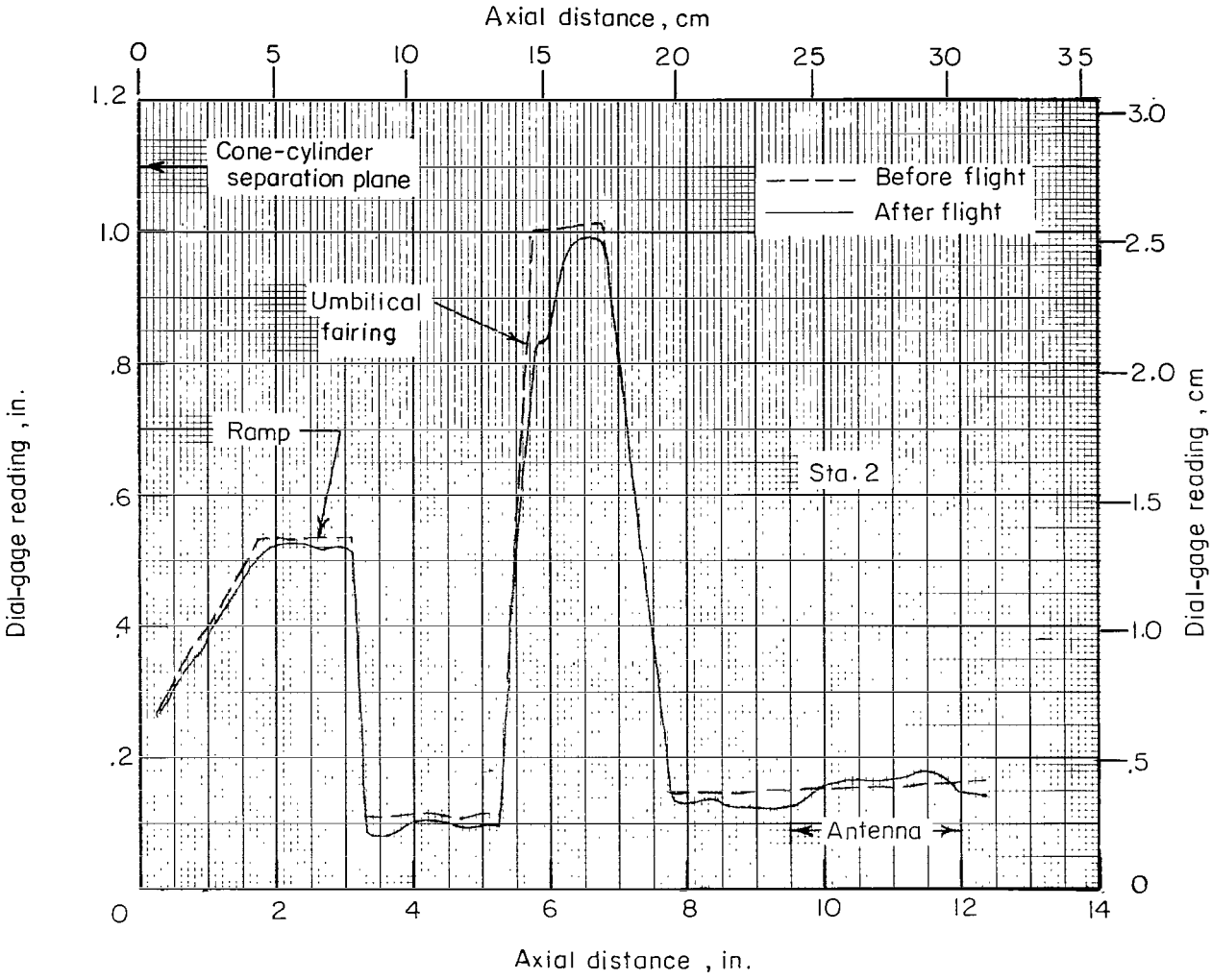

(c) Station 2.

Figure 19.- Continued.

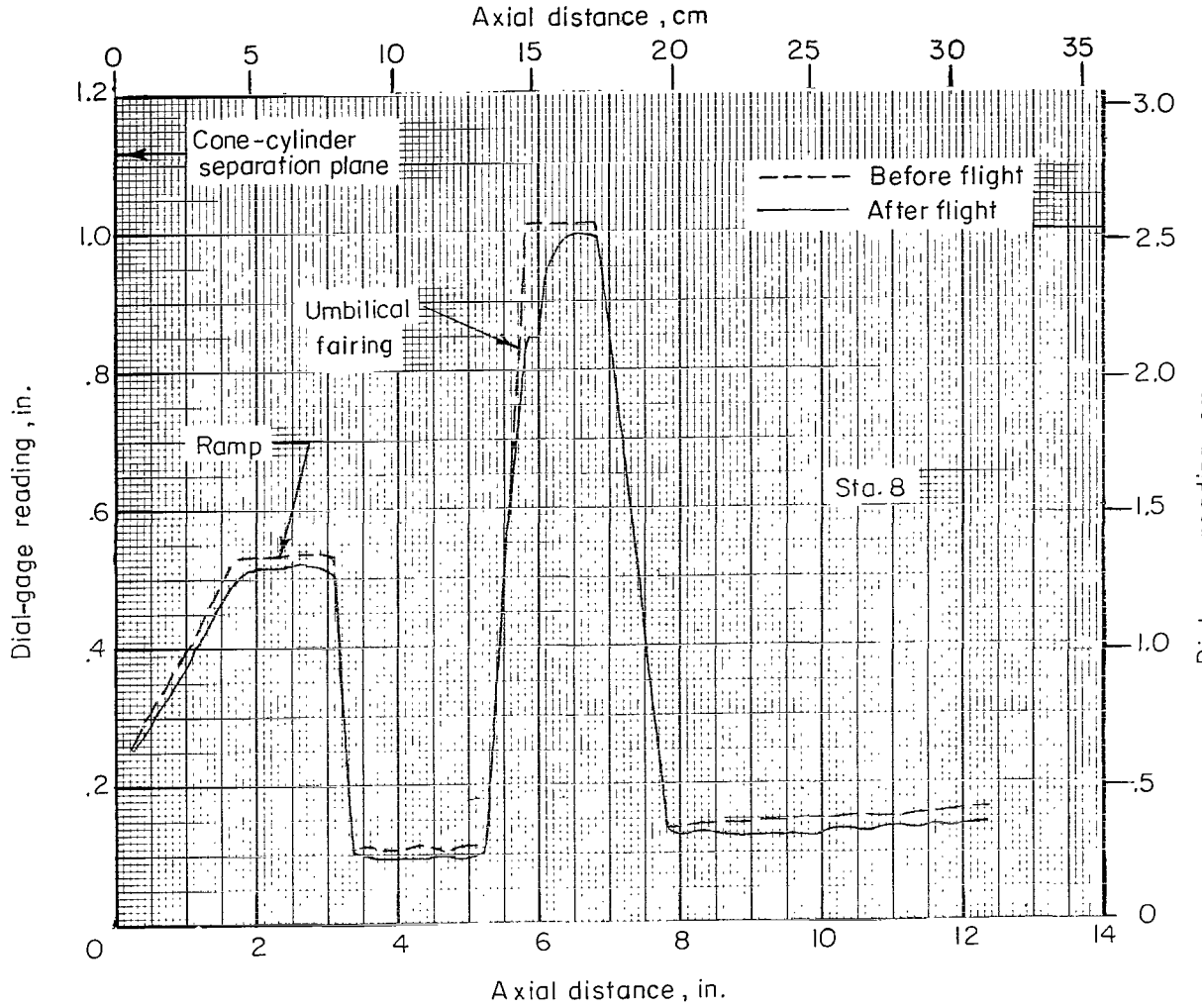

(d) Station 8.

Figure 19.- Continued.

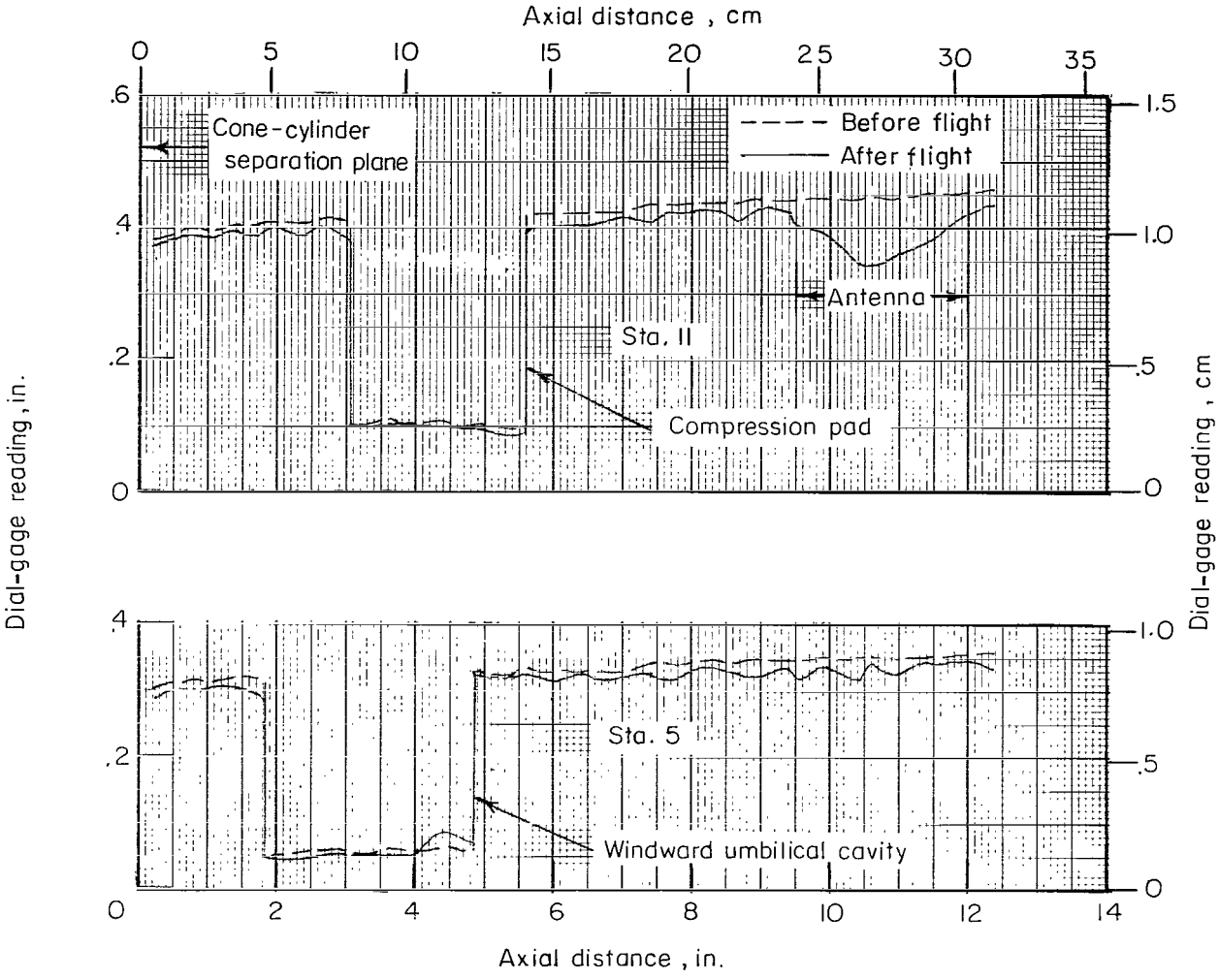

(e) Stations 11 and 5.

Figure 19.- Concluded.

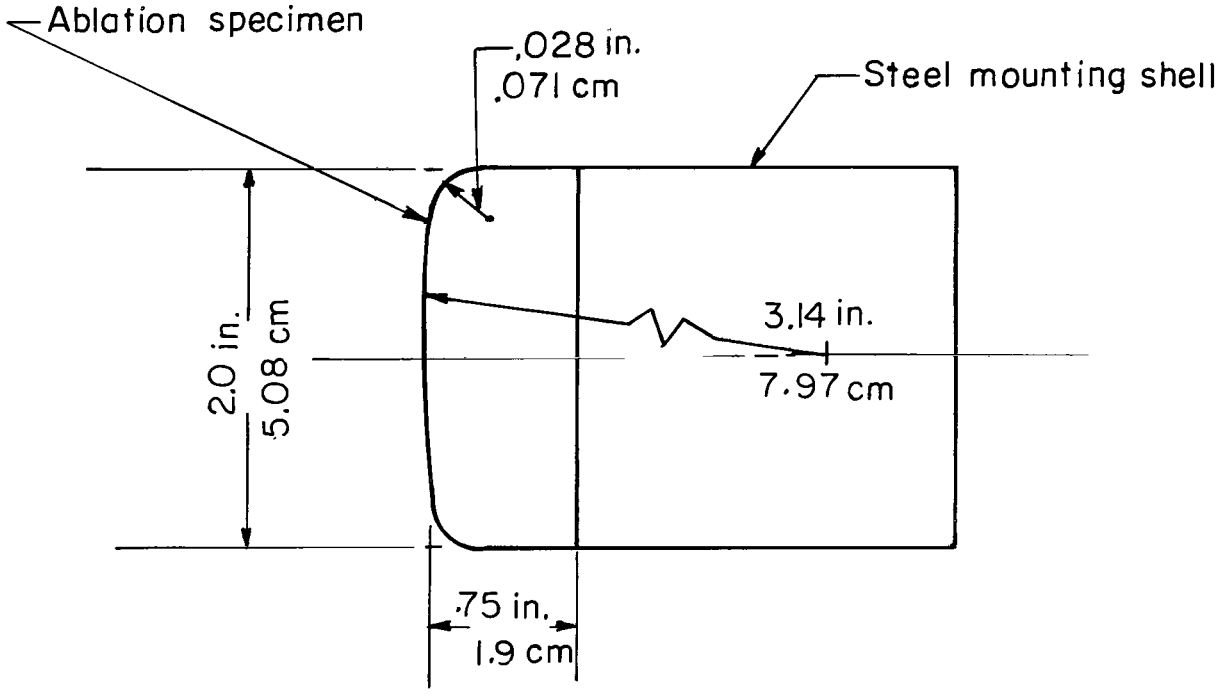

Figure 20.- Sketch of arc-jet test models.

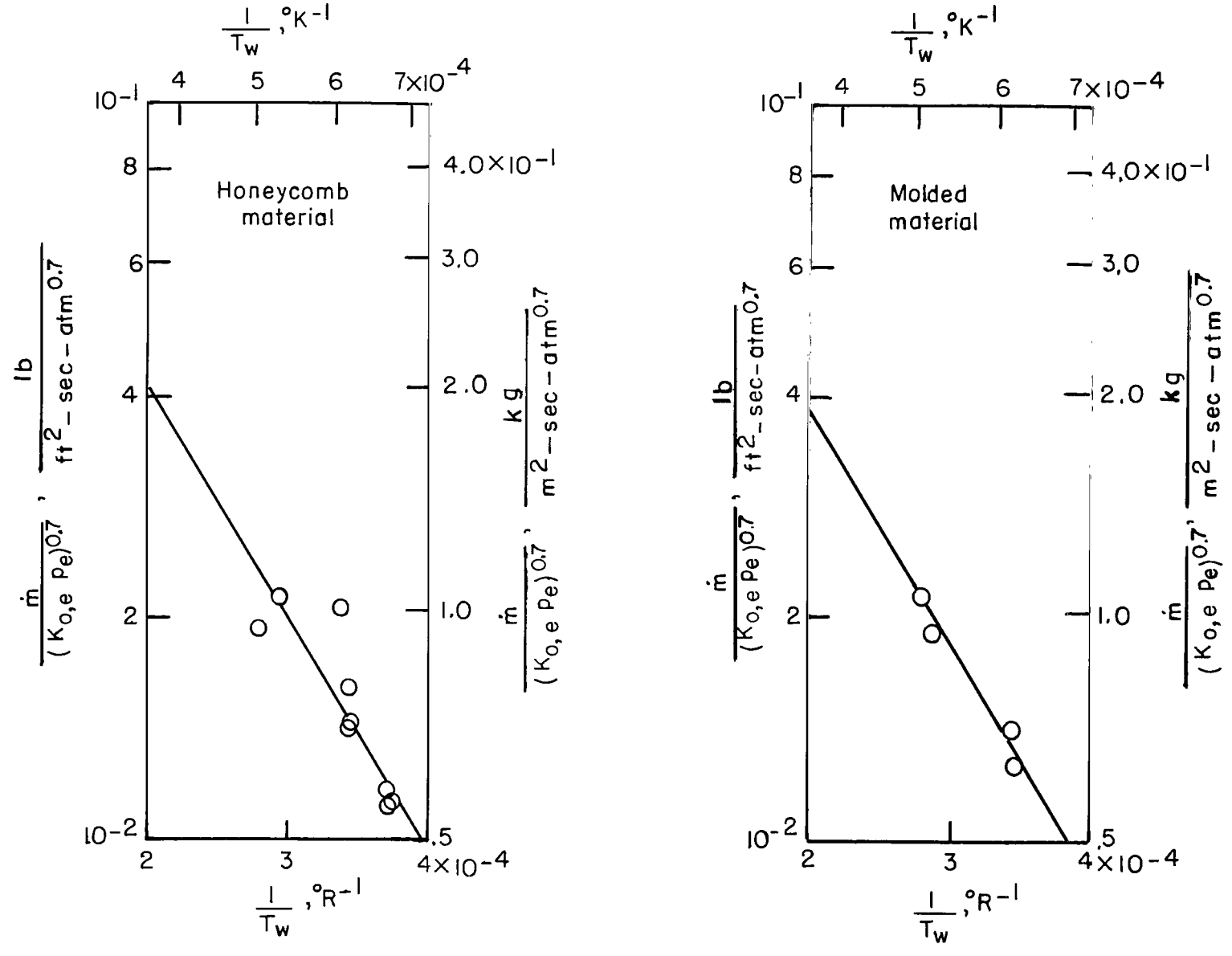

Figure 21.- Arrhenius plots of arc-jet test data for molded- and composite-ablator materials.

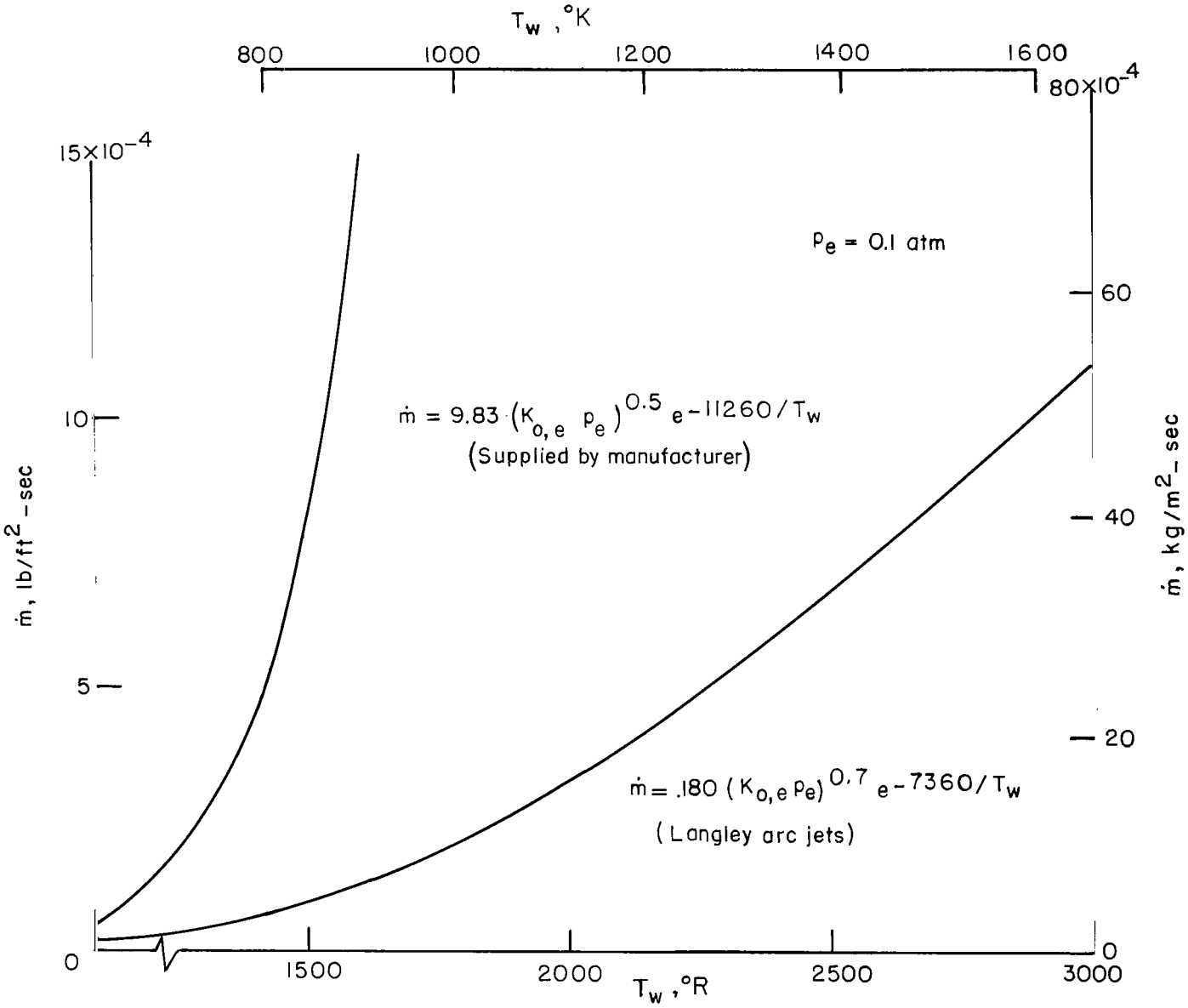

Figure 22.- Comparison of Arrhenius equations from both arc-jet tests and ablator manufacturer.

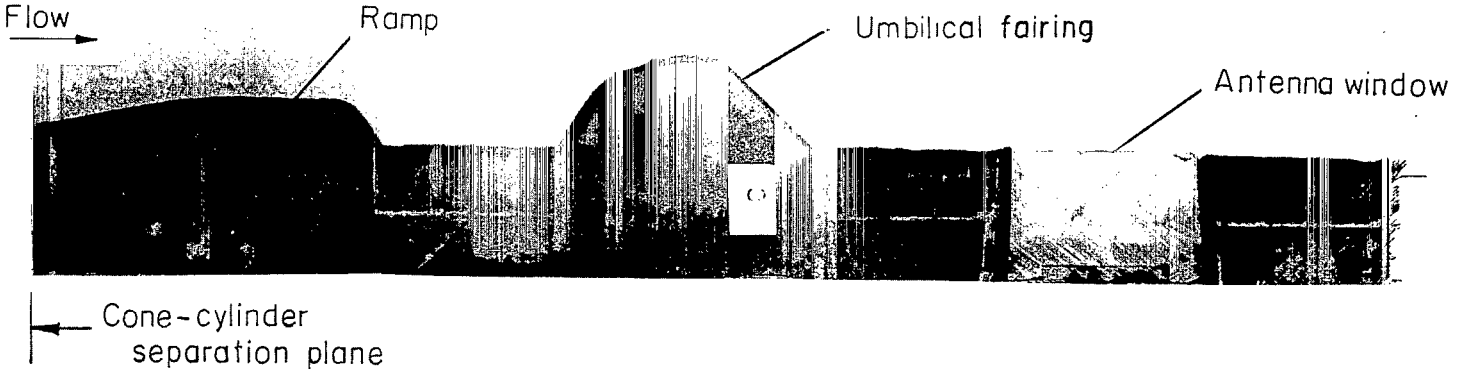

(a) Composite-ablator quadrant. L-66-9467.1

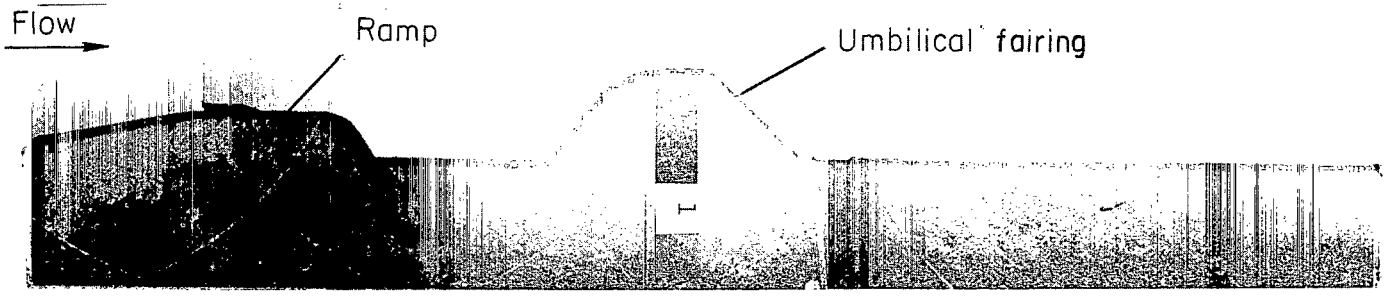

(b) Molded-ablator quadrant. L-66-9463.1

Figure 23.- Photographs of the sectioned ramp-umbilical simulation.

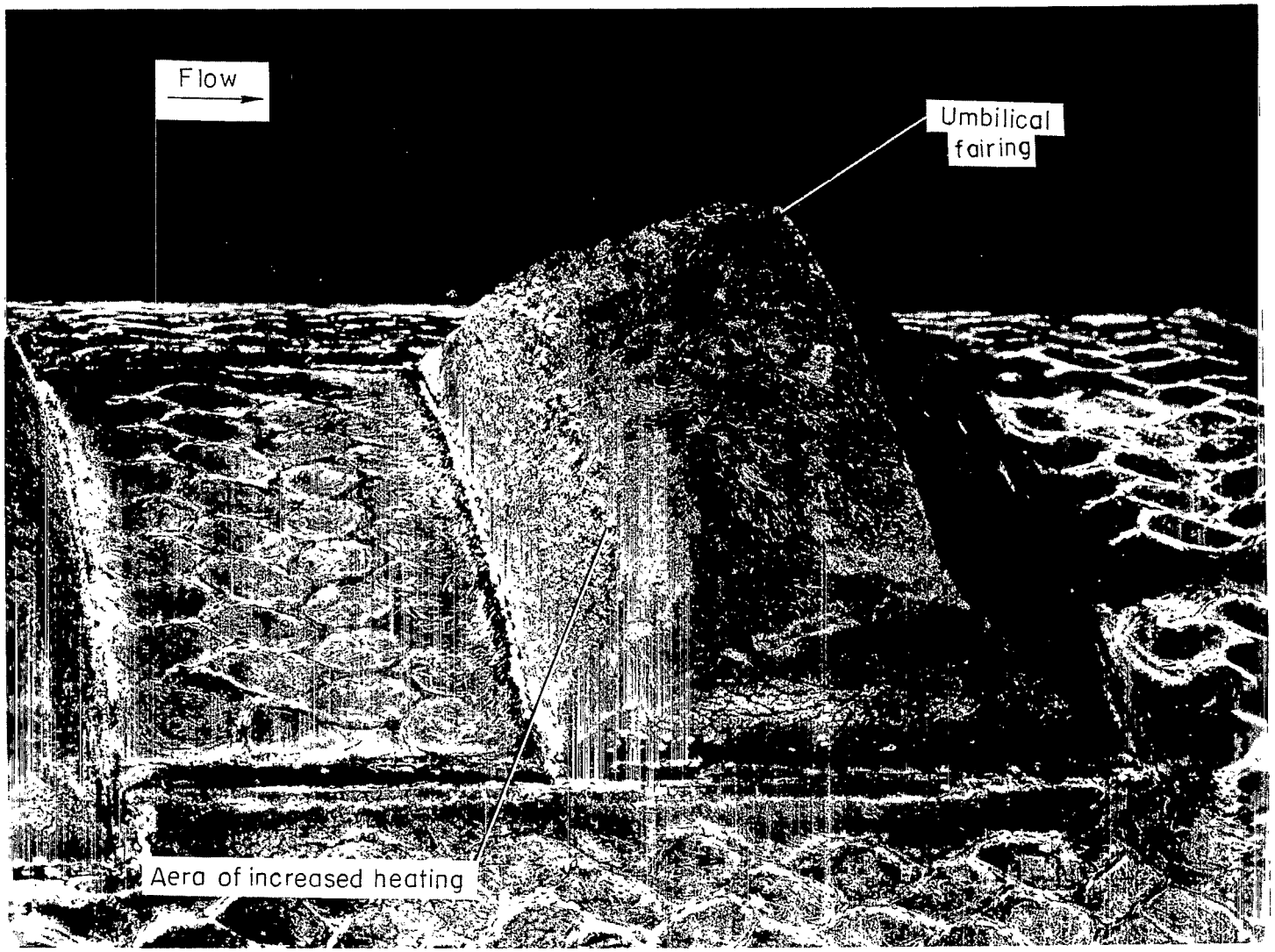

(a) Composite-ablator quadrant. L-66-8969.1

Figure 24.- Photographs of umbilical simulation.

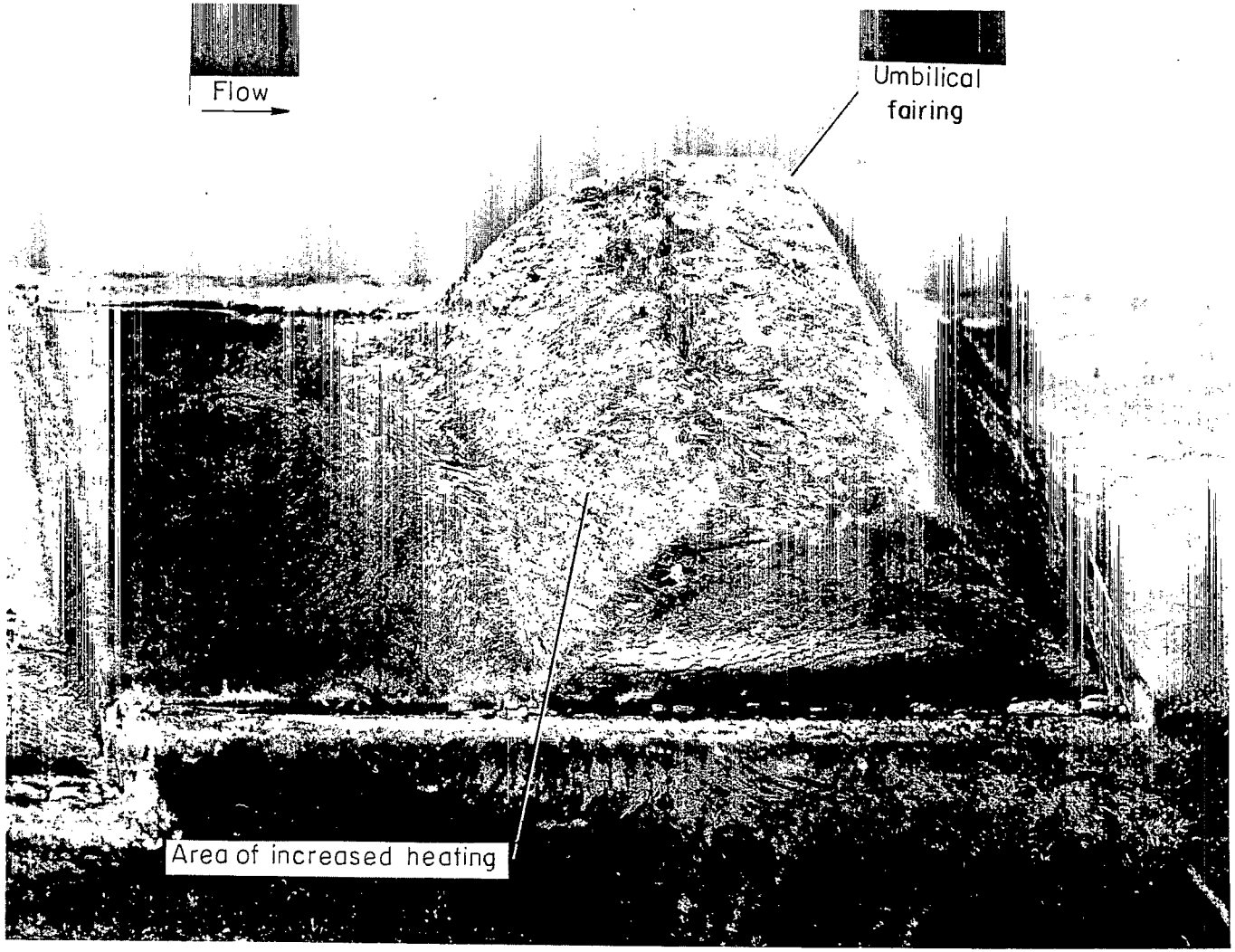

(b) Molded-ablator quadrant.

L-66-8974.1

Figure 24.- Concluded.

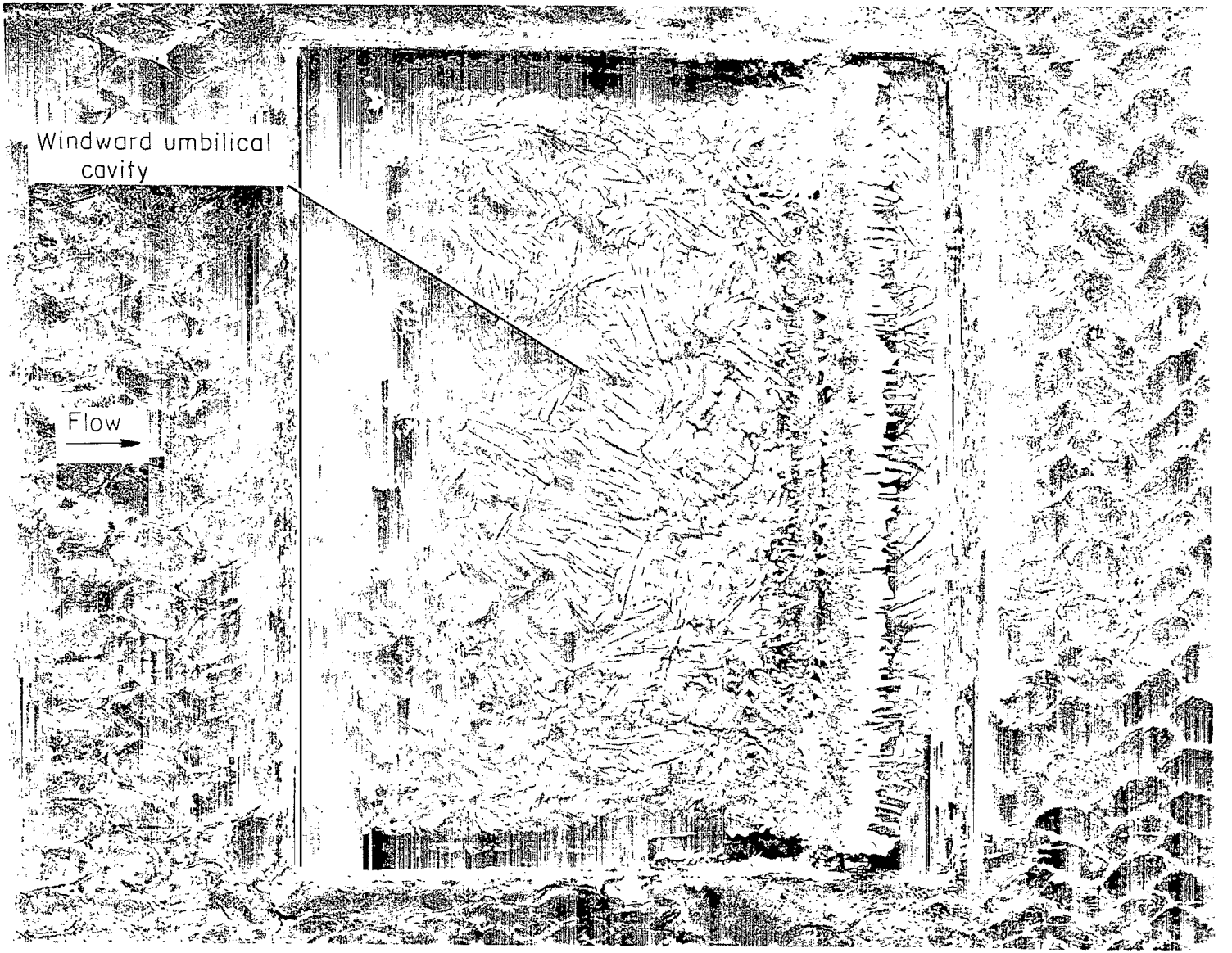

Figure 25.- Photograph of windward-umbilical-cavity simulation (enlarged).

L-66-8967.1

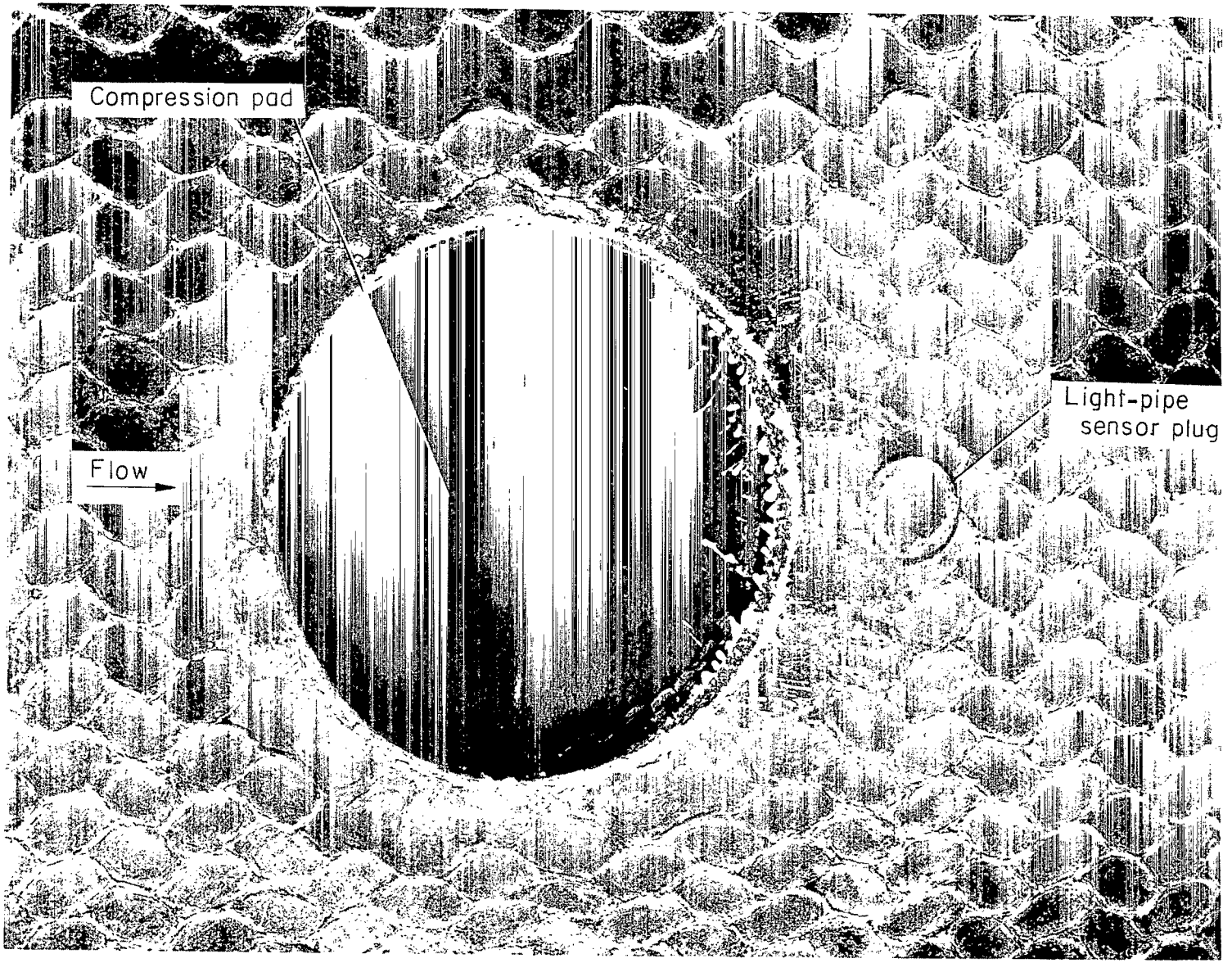

Figure 26.- Photograph of compression-pad simulation (enlarged).

L-66-8973.1

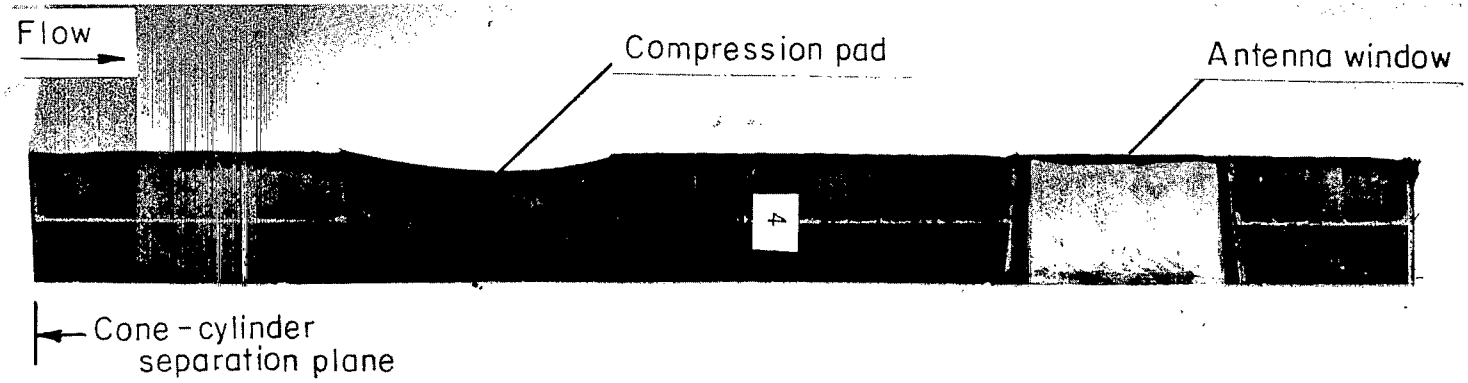

(a) Compression-pad simulation. L-66-9479.1

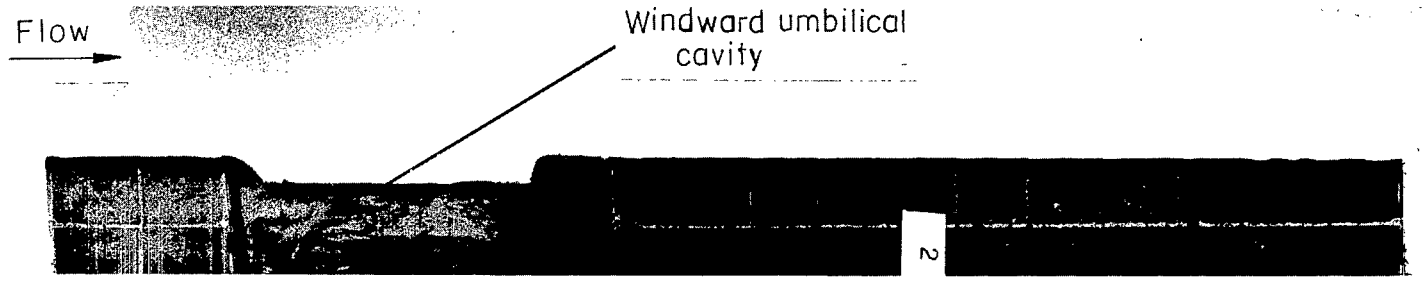

(b) Windward-umbilical-cavity simulation. L-66-9464.1

Figure 27.- Photographs of the sectioned compression-pad and windward-umbilical-cavity simulations.

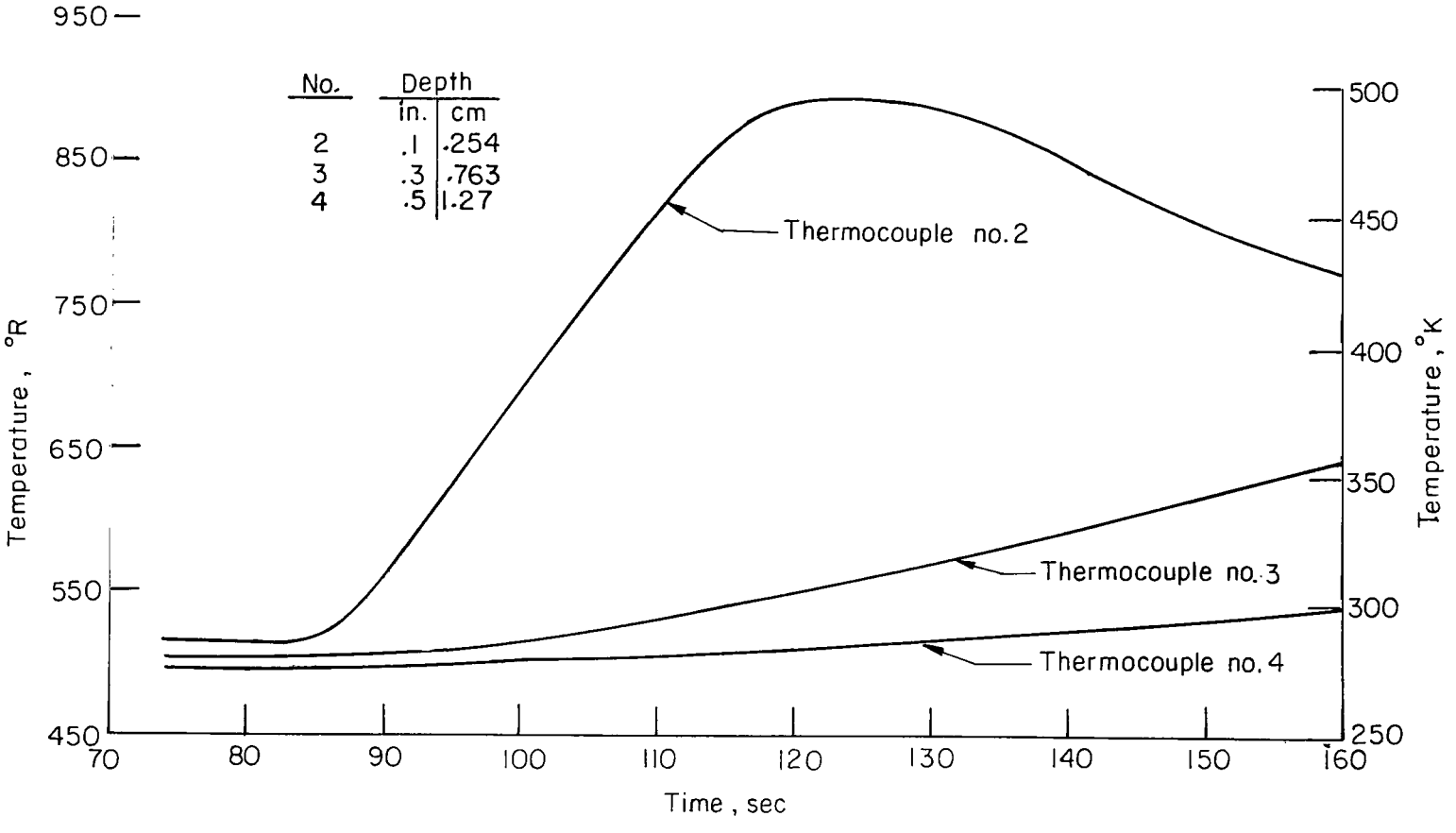

Figure 28.- Time histories of the temperature at several depths in windward-umbilical-cavity simulation.

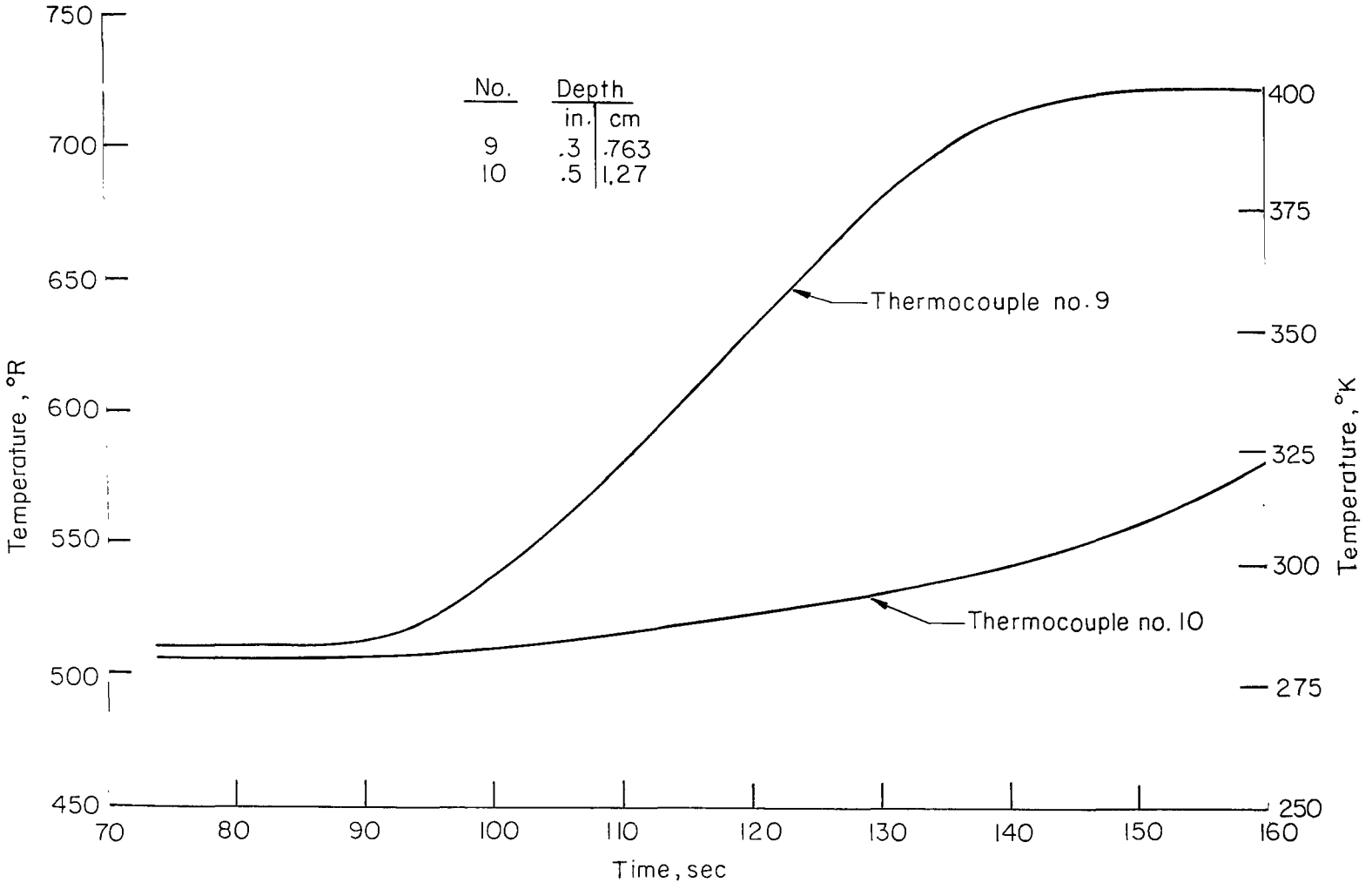

Figure 29.- Time histories of the temperature at several depths in compression-pad simulation.

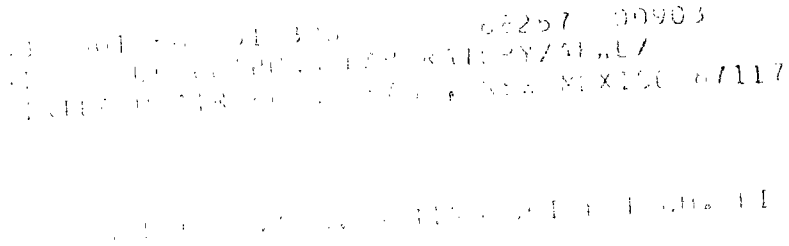

"The aeronautical and space activities of the United States shall be conducted so as to contribute . . . to the expansion of human knowledge of phenomena in the atmosphere and space. The Administration shall provide for the widest practicable and appropriate dissemination of information concerning its activities and the results thereof."

—NATIONAL AERONAUTICS AND SPACE ACT OF 1958

NASA SCIENTIFIC AND TECHNICAL PUBLICATIONS

TECHNICAL REPORTS: Scientific and technical information considered important, complete, and a lasting contribution to existing knowledge.

TECHNICAL NOTES: Information less broad in scope but nevertheless of importance as a contribution to existing knowledge.

TECHNICAL MEMORANDUMS: Information receiving limited distribution because of preliminary data, security classification, or other reasons.

CONTRACTOR REPORTS: Scientific and technical information generated under a NASA contract or grant and considered an important contribution to existing knowledge.

TECHNICAL TRANSLATIONS: Information published in a foreign language considered to merit NASA distribution in English.

SPECIAL PUBLICATIONS: Information derived from or of value to NASA activities. Publications include conference proceedings, monographs, data compilations, handbooks, sourcebooks, and special bibliographies.

TECHNOLOGY UTILIZATION PUBLICATIONS: Information on technology used by NASA that may be of particular interest in commercial and other non-aerospace applications. Publications include Tech Briefs, Technology Utilization Reports and Notes, and Technology Surveys.

Details on the availability of these publications may be obtained from:

SCIENTIFIC AND TECHNICAL INFORMATION DIVISION

NATIONAL AERONAUTICS AND SPACE ADMINISTRATION

Washington, D.C. 20546